All-sky search for continuous gravitational waves from isolated neutron stars using Advanced LIGO O2 data

B.P. Abbott, R. Abbott, T.D. Abbott, S. Abraham, F. Acernese, K. Ackley, C. Adams, R.X. Adhikari, V.B. Adya, C. Affeldt, et al.

All-sky search for continuous gravitational waves from isolated neutron stars using Advanced LIGO O2 data

B. P. Abbott *et al.*[*]
(LIGO Scientific Collaboration and Virgo Collaboration)

(Received 15 March 2019; published 8 July 2019)

We present results of an all-sky search for continuous gravitational waves (CWs), which can be produced by fast spinning neutron stars with an asymmetry around their rotation axis, using data from the second observing run of the Advanced LIGO detectors. Three different semicoherent methods are used to search in a gravitational-wave frequency band from 20 to 1922 Hz and a first frequency derivative from -1×10^{-8} to 2×10^{-9} Hz/s. None of these searches has found clear evidence for a CW signal, so upper limits on the gravitational-wave strain amplitude are calculated, which for this broad range in parameter space are the most sensitive ever achieved.

DOI: 10.1103/PhysRevD.100.024004

I. INTRODUCTION

Eleven detections of gravitational waves from black hole binaries and from a neutron star binary have been reported in [1]. One of the characteristics of the signals detected so far is that their duration ranges from a fraction of a second to tens of seconds in the detector sensitive frequency band. Other mechanisms, however, can produce gravitational waves with longer durations, not yet detected. In this paper we describe an all-sky search for continuous gravitational waves (CWs), almost monochromatic signals which are present at the detectors during all the observing time. The principal sources for CW emission (see [2] for a review) are spinning neutron stars. If a spinning neutron star (NS) has an asymmetry with respect to its rotation axis, it will emit CWs at twice the rotation frequency.

Fast-spinning neutron stars in the Milky Way can generate continuous gravitational waves via various processes which produce an asymmetry. Crustal distortions from cooling or from binary accretion, or magnetic field energy buried below the crust could lead to the nonaxisymmetry necessary for detectable emission. The excitation of r-modes in a newborn or accreting NS is another promising mechanism for the emission of CWs. Recently, some evidence for a limiting minimum ellipticity was discussed in [3]. A comprehensive review of continuous gravitational wave emission mechanisms from neutron stars can be found in [4]. The detection of a CW, possibly combined with electromagnetic observations of the same source, could yield insight into the structure of neutron stars and into the equation of state of matter under extreme conditions.

Searches for continuous waves are usually split in three different domains: targeted searches look for signals from known pulsars [5–15]; directed searches look for signals from known sky locations like the Galactic Center, supernova remnants and low-mass x-ray binaries such as Sco-X1 [16–26]; all-sky searches look for signals from unknown sources [27–40]. Since all-sky searches need to cover a large parameter space, they are the most computationally expensive. For this reason, the most sensitive coherent search methods (e.g., matched filtering for the full observing run) cannot be used and semicoherent methods which split the full observation time in shorter chunks need to be used.

The interest in all-sky searches stems from the fact that they inspect regions of parameter space that no other searches look at. Although the targeted searches are more sensitive, they are limited to search for known pulsars which are in the sensitive frequency band of the detectors, while all-sky searches look for neutron stars with no electromagnetic counterpart, which could have different or more extreme properties than the observed pulsars.

In this paper we present the results of an all-sky search of CWs by three different pipelines (*FrequencyHough* [41], *SkyHough* [42], *Time-Domain $\mathcal{F}$-statistic* [43]) using O2 data from the Advanced LIGO detectors. Each pipeline uses different data analysis methods and covers different regions of the parameter space, although there exists some overlap between them. Overall, we search the whole sky for gravitational wave frequencies from 20 to 1922 Hz (this number was chosen in order to avoid the violin modes of the test masses found at higher frequencies) and a first frequency derivative from -1×10^{-8} to 2×10^{-9} Hz/s (positive frequency derivatives are possible for neutron stars which are spun up by accretion from a companion). No detection has been made, and upper limits on the gravitational wave amplitude are presented.

The outline of the paper is the following: in Sec. II, we summarize the second observing run and give some details

[*]Full author list given at the end of the article.

about the data that is used; in Sec. III, we describe the model of the signal that we want to detect; in Sec. IV, we present the different pipelines which are used; in Sec. V, we describe the results obtained by each pipeline; in Sec. VI, we give some final remarks.

II. LIGO O2 OBSERVING RUN

The LIGO second observing run (called O2) started on November 30, 2016 and finished on August 25, 2017. During this time, three different gravitational-wave detectors of second generation were active and producing data: Advanced LIGO [44], consisting of two detectors with 4-km arm lengths situated in Hanford, Washington (H1) and Livingston, Louisiana (L1), and Advanced Virgo [45], a 3-km detector located in Cascina, Pisa. Advanced Virgo first joined the run at the beginning of August 2017, with less sensitivity than the LIGO detectors, so we have not considered its data for the search described in this paper.

A representative noise curve from O2 for each LIGO detector and a comparison to O1 is shown in Fig. 1. We can observe an improvement of the amplitude spectral density, and we can also observe that the spectra features a number (greatly reduced as compared to O1) of narrow lines and combs affecting several frequency bands, which contaminate the data and complicate the analysis often raising outliers which look like the searched CW signals [46]. A cleaning procedure was applied to H1 data during postprocessing in order to remove jitter noise and some noise lines (more details are given in [47]). All of the searches of this paper used this cleaned dataset. The calibration of this dataset and its uncertainties on amplitude and phase are described in [48]. These searches do not use all the data from the observing run, since times where the detectors are known to be poorly behaving are removed from the analysis. This means that the effective amount of data used is smaller than the full duration of the run. As in previous observing runs, several artificial signals (called hardware injections) have been physically injected in the detectors in order to test their response and to validate the different pipelines. These hardware injections are described in Secs. III, V and in the Appendix.

III. SIGNAL MODEL

An asymmetric neutron star spinning around one of its principal axes of inertia emits a CW signal at twice its rotation frequency. This emission is circularly polarized along the rotation axis and linearly polarized in the directions perpendicular to the rotation axis. The gravitational-wave signal in the detector frame is given by [43]

$$h(t) = h_0\left[F_+(t)\frac{1+\cos\iota}{2}\cos\phi(t) + F_\times(t)\cos\iota\sin\phi(t)\right], \tag{1}$$

where $F_+(t)$ and $F_\times(t)$ are the antenna patterns of the detectors (which can be found in [43]), h_0 is the amplitude of the signal, ι is the inclination of the neutron star angular momentum vector with respect to the observer's sky plane, and $\phi(t)$ is the phase of the signal. The amplitude of the signal is given by

$$h_0 = \frac{4\pi^2 G}{c^4}\frac{I_{zz}\epsilon f^2}{d}, \tag{2}$$

where d is the distance from the detector to the source, f is the gravitational-wave frequency, ϵ is the ellipticity or asymmetry of the star, given by $(I_{xx}-I_{yy})/I_{zz}$, and I_{zz} is the moment of inertia of the star with respect to the principal axis aligned with the rotation axis. These two last quantities are related to the mass quadrupole moment Q_{22} of the star:

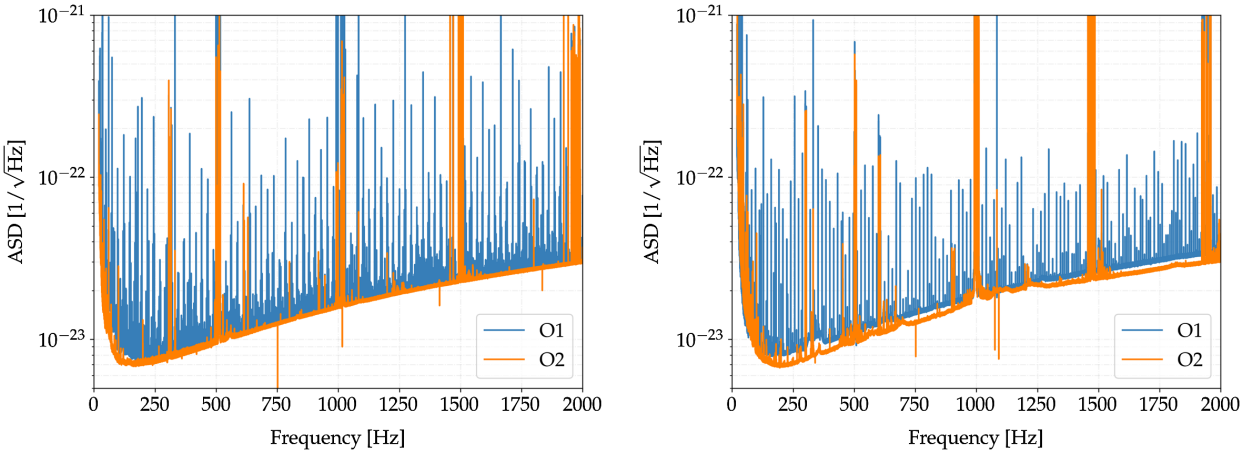

FIG. 1. Amplitude spectral density (ASD) $\sqrt{S_n}$ plots for the L1 (left panel) and H1 (right panel) detectors during O1 (blue trace) and O2 (orange trace). The ASD is obtained by averaging over FFTs of 1800 s obtained for the entire run.

$$\epsilon = \sqrt{\frac{8\pi}{15}}\frac{Q_{22}}{I_{zz}}. \quad (3)$$

We assume that the phase evolution of the gravitational-wave signal, which is locked to the evolution of the rotational frequency, can be approximated with a Taylor expansion (assumption taken from electromagnetic observations of pulsars) around a fiducial reference time τ_r:

$$\phi(\tau) = \phi_0 + 2\pi\left[f_0(\tau-\tau_r) + \frac{\dot{f}}{2!}(\tau-\tau_r)^2 + \cdots\right], \quad (4)$$

where ϕ_0 is an initial phase and f_0 and $\dot{f}$ are the frequency and first frequency derivative at the reference time. The relation between the time at the source τ and the time at the detector t is given by (neglecting relativistic effects like the Einstein and Shapiro delays)

$$\tau(t) = t + \frac{\vec{r}(t)\cdot\hat{n}}{c}, \quad (5)$$

where $r(t)$ is the vector which joins the Solar System barycenter (SSB) and the detector, and $\hat{n}$ is the vector identifying the star's position in the SSB. From the previous formula the frequency evolution of the signal can be derived as

$$f(t) = \frac{1}{2\pi}\frac{d\phi}{dt} \simeq f_0 + f_0\frac{\vec{v}(t)\cdot\hat{n}}{c} + \dot{f}t. \quad (6)$$

The second term in the right-hand side of this equation describes the frequency modulation due to the Doppler effect produced by Earth's rotation and translation around the SSB. This term, together with the spin-down/up of the source, must be properly taken into account when carrying out the search.

Equations (4) through (6) assume that the neutron star is isolated. In case it is part of a binary system, the frequency evolution is complicated by the binary system orbital motion, which introduces an additional frequency modulation. Such modulation, on a signal of frequency f and neglecting the binary system ellipticity, is given by (see [49])

$$\Delta f_{\rm orb} \simeq \frac{2\pi}{P} a_p f, \quad (7)$$

where P is the binary orbital period and a_p is the projected orbital semimajor axis (in light-seconds). By imposing that the orbital frequency modulation is contained into a frequency bin $\delta f = 1/T_{FFT}$, where T_{FFT} is the duration of the data chunks which are incoherently combined in the analysis (see Sec. IV), we find that two of the search pipelines (*FrequencyHough* and *SkyHough*) used in this paper would be fully sensitive to a CW signal from a NS in a binary system if

$$a_p \ll 0.076\left(\frac{P}{1\ \text{day}}\right)\left(\frac{f}{100\ \text{Hz}}\right)^{-1}\left(\frac{T_{FFT}}{1800\ \text{s}}\right)^{-1}\ \text{s}. \quad (8)$$

For larger orbital frequency modulations the pipelines would start to lose signal-to-noise ratio but a detailed study of this issue is outside the scope of the paper. Out of 259 pulsars in binary systems from the australia telescope national facility catalogue, only six of them have such characteristics, although many undiscovered neutron stars in binary systems could also be part of systems with these properties.

IV. DESCRIPTION OF THE SEARCH METHODS

In this section we introduce and summarize the three different pipelines which have been used in this work.

A. FrequencyHough

The *FrequencyHough* pipeline consists of an initial multistep phase, in which interesting points (i.e., candidates) are selected in the signal parameter space, and of a subsequent follow-up stage to confirm or reject the candidates. A complete description of the method and of the fundamental implementation features are given in [41,50]. Upper limits are computed with a frequentist approach, by injecting a large number of simulated signals into the data. The pipeline has been previously used in all-sky searches of Virgo VSR2, VSR4 [36] and LIGO O1 Science Runs data [38].

1. Initial analysis steps

The starting point of the analysis is calibrated detector data, used to create "short duration" fast Fourier transforms (FFTs) with coherence time depending on the frequency band being considered, according to Table I. Short time-domain disturbances are removed from the data before constructing the FFTs [51]. Next, a time-frequency map, called peakmap, is built by identifying local maxima (called peaks) above a dimensionless threshold $\theta_{\rm thr} = 1.58$ on the

TABLE I. Properties of the FFTs used in the *FrequencyHough* pipeline. The time duration $T_{\rm FFT}$ refers to the length in seconds of the data chunks on which the FFT is computed. The frequency bin width is the inverse of the time duration, while the spin-down/up bin width is computed as $\delta\dot{f} = \delta f/T_{\rm obs}$, where $T_{\rm obs}$ is the total run duration. In the analysis described in this paper only the first three bands have been considered, the last one will be analyzed in a future work. The spin-down/up range covered by the analysis is $(+2\times10^{-9}$ Hz/s, -10^{-8} Hz/s) up to 512 Hz and $(+2\times10^{-9}$ Hz/s, -2×10^{-9} Hz/s) from 512 Hz up to 1024 Hz.

Band [Hz]	$T_{\rm FFT}$ [s]	δf [Hz]	$\delta\dot{f}$ [Hz/s]
10–128	8192	1.22×10^{-4}	5.26×10^{-12}
128–512	4096	2.44×10^{-4}	1.05×10^{-11}
512–1024	2048	4.88×10^{-4}	2.10×10^{-11}
1024–2048	1024	9.76×10^{-4}	4.20×10^{-11}

square root of the equalized power[1] of the data [51]. The peakmap is cleaned using a line *persistency* veto [41], based on the projection of the peakmap onto the frequency axis and on the removal of the frequency bins in which the projection is higher than a given threshold.

After defining a grid in the sky, with bin size depending on the frequency and sky location as detailed in [41], the time-frequency peaks are properly shifted, for each sky position, to compensate the Doppler effect due to the detector motion, see Eq. (6). They are then processed by the *FrequencyHough* algorithm [41,50], which transforms each peak to the frequency and spin-down/up plane of the source. The frequency and spin-down/up bins (which we will refer to as *coarse* bins in the following) depend on the frequency band, as indicated in Table I, and are defined, respectively, as $\delta f = \frac{1}{T_{\mathrm{FFT}}}$ and $\delta \dot{f} = \delta f / T_{\mathrm{obs}}$, where $T_{\mathrm{obs}} = 268.37$ days is the total run duration. In practice, as the transformation from the peakmap to the Hough plane is not computationally bounded by the width of the frequency bin, we have increased the nominal frequency resolution by a factor of 10 [41]. The algorithm, moreover, properly weights any noise nonstationarity and the time-varying detector response [52].

The *FrequencyHough* transform is computationally very demanding, so the analysis is split into tens of thousands of independent jobs, each of which computes a *FrequencyHough* transform covering a small portion of the parameter space. The output of a *FrequencyHough* transform is a 2D histogram in the frequency/spin-down plane of the source. Candidates for each sky location are selected by dividing each 1-Hz band of the corresponding *FrequencyHough* histogram into 20 intervals and taking, for each interval, the one or (in most cases) two candidates with the highest histogram number count. This allows us to avoid blinding by large disturbances in the data, as described in [41]. All the steps described so far are applied separately to the data of each detector involved in the analysis.

Following the same procedure used in [38], candidates from each detector are clustered and then coincident candidates among the clusters of the two detectors are found using a distance metric built in the four-dimensional parameter space of position (λ, β) (in ecliptic coordinates), frequency f and spin-down/up $\dot{f}$, defined as

$$d_{\mathrm{FH}} = \sqrt{\left(\frac{\Delta f}{\delta f}\right)^2 + \left(\frac{\Delta \dot{f}}{\delta \dot{f}}\right)^2 + \left(\frac{\Delta \lambda}{\delta \lambda}\right)^2 + \left(\frac{\Delta \beta}{\delta \beta}\right)^2}, \quad (9)$$

where Δf, $\Delta \dot{f}$, $\Delta \lambda$, and $\Delta \beta$ are the differences, for each parameter, among pairs of candidates of the two detectors, and δf, $\delta \dot{f}$, $\delta \lambda$, and $\delta \beta$ are the corresponding bin widths. Pairs of candidates with distance $d_{\mathrm{FH}} < 3$ are considered coincident. This value was chosen based on a study with software simulated signals and allows, on one hand, to reduce the false alarm probability and, on the other, to be sufficiently robust with respect to the fact that a signal can be found with slightly different parameters in the two detectors. Coincident candidates are subject to a ranking procedure, based on the value of a statistic built using the distance and the *FrequencyHough* histogram weighted number count of the coincident candidates, as described in [41]. In this analysis, after the ranking the eight candidates in each 0.1-Hz band with the highest values of the statistic have been selected.

2. Candidate follow-up

Candidates passing the ranking selection are followed up in order to confirm them as potential CW signals or to discard them, if due to noise fluctuations or detector disturbances. The follow-up consists of several steps, as described in [36]. An important implementation novelty we have introduced in the O2 analysis is the use of the *Band Sampled Data* framework (BSD) [53], which allows a flexible and computationally efficient management of the data. For each of the N candidates selected by the ranking procedure, a fully coherent search is done using down-sampled data from both detectors, covering a band of the order of 0.2 Hz around the candidate frequency. The coherent search is done by applying a Doppler and spin-down/up correction based on the parameters of the candidate. Although the coherent search corrects exactly for the Doppler and spin-down/up effect at a particular point in the parameter space, corresponding to the candidate, the correction is extended by linear interpolation to the neighbors of the candidate itself. In practice, this means that from the corrected and down-sampled time series, a new set of FFTs

TABLE II. Properties of the FFTs used in the *FrequencyHough* follow-up step. The second column is the increased FFT duration, the third is the enhancement factor $\mathcal{E}$, with respect to the original duration. The fourth and fifth columns show, respectively, the new frequency and spin-down/up bins, while the sixth is the estimated sensitivity gain $\mathcal{G}$. The new durations have been chosen in such a way to avoid the effect of the sidereal modulation, which produces a spread of the signal power in frequency sidebands [54]. Actually, for the third band we have used a shorter duration due to computer memory constraints. The last band, from 1024 to 2048 Hz, has not been considered in this work.

Band [Hz]	FFT duration [s]	$\mathcal{E}$	δf [Hz]	$\delta \dot{f}$ [Hz/s]	$\mathcal{G}$
10–128	24600	3	4.07×10^{-5}	1.75×10^{-2}	1.39
128–512	24576	6	4.07×10^{-5}	1.75×10^{-12}	1.65
512–1024	8192	4	1.22×10^{-4}	5.26×10^{-12}	1.49

[1]Defined as the ratio of the squared modulus of the FFT of the data and an autoregressive estimation of the power spectrum, see [51] for more details.

is built, with a longer duration (by a varying factor $\mathcal{E}$, depending on the frequency band, see Table II), as well as the corresponding peakmap. Peaks are selected using a threshold $\theta_{\rm thr} = 1.87$, bigger than the initial one (see Sec. IV A). As explained in [36] this is a conservative choice which provides a sensitivity gain and, at the same time, reduces the computational cost of the follow-up. As a result of the FFT length increase and of the new threshold for the selection of the peaks, by using Eq. (67) of [41], which is valid under the assumption of Gaussian noise, we estimate a sensitivity gain $\mathcal{G}$ for the detectable h_0 in the follow-up, shown in the last column of Table II. A small area, centered around the candidate position, is considered for the follow-up. It covers ± 3 coarse bins, which amounts to seven bins in each dimension, and thus 49 coarse sky positions for each candidate. A refined sky grid is built over this area, with an actual number of points which depends on the frequency band and is, on the average, given by $49\mathcal{E}^2$. For each sky position in this refined grid, we evaluate the residual Doppler modulation (with respect to the center of the grid), which is corrected in the peakmap by properly shifting each peak. The *FrequencyHough* of the resulting ensemble of corrected peakmaps is computed over a frequency and spin-down/up ranges covering ± 3 coarse bins around the candidate values. As before, an over-resolution factor of 10 is used for the frequency. The absolute maximum identified over all the Hough maps provides the refined parameters of the candidate we are considering. Next, to each pair of candidates from the two detectors we apply a series of vetoes, as detailed in the following.

First, we remove the candidates whose median value of the frequency (computed over the full observing time), after the removal of the Doppler and spin-down/up correction, overlaps a known noise line frequency band (i.e., a line due to a detector disturbance, whose instrumental origin has been understood). Second, for each detector a new peakmap is computed using the data coherently corrected with the refined parameters of the candidate and then projected on the frequency axis. We take the maximum A_p of this projection in a range of ± 2 coarse bins around the candidate frequency. We divide the rest of the 0.2 Hz band (which we consider the "off-source" region) into ~ 250 intervals of the same width, take the maximum of the peakmap projection in each of these intervals and sort in decreasing order all these maxima. We tag the candidate as "interesting" and keep it if it ranks first or second in this list for both detectors. Surviving candidates are then subject to a consistency test based on their critical ratio, defined as $\mathrm{CR} = (A_p - \mu_p)/\sigma_p$, where μ_p and σ_p are the mean and standard deviation of the peakmap projection on the off-source region. Pairs of coincident candidates are removed if their CRs, properly weighted by the detector noise level at the candidate frequency, differ by more than a factor of 5. Further details on O2 outlier selection and properties are given in Sec. V A.

3. Upper limit computation

Upper limits are computed in each 1-Hz band between 20 and 1000 Hz by injecting software simulated signals, with the same procedure used in [36]. For each 1 Hz band 20 sets of 100 signals each are generated, with fixed amplitude within each set and random parameters (sky location, frequency, spin-down/up, and polarization parameters). These are generated in time domain and then added to the data of both detectors in the frequency domain. For each injected signal in a set of 100, an analysis is done using the *FrequencyHough* pipeline over a frequency band of 0.1 Hz around the injection frequency, the full spin-down/up range used in the real analysis, and nine sky points around the injection position [36]. Candidates are selected as in the real analysis, except that no clustering is applied, as it would have been affected by the presence of too many signals. We note, however, that clustering is used in the analysis only to reduce the computational cost and does not affect the subsequent steps. After coincidences and ranking, candidates also coincident with the injected signal parameters, within the follow-up volume discussed in Sec. IV A 2, are selected. Those having a critical ratio larger than the largest critical ratio found in the real analysis in the same 1 Hz are counted as *detections*. For each 1 Hz band, we build the detection efficiency curve, defined as the fraction of detected signals as a function of their amplitude. The upper limit is given by the signal amplitude such that the detection efficiency is 95%. In practice, a fit is used in order to interpolate the detection efficiency curve, as described in [38].

B. SkyHough

The *SkyHough* method has been used in other searches using data from the Initial LIGO S2, S4 and S5 and Advanced LIGO O1 observing runs [27,28,32,38,40]. Its main description is given in [42]. Here we summarize its main characteristics and the new features that have been implemented in this search. The code for the main part of the search is called *lalapps_DriveHoughMulti* and is part of the publicly available LALSuite package [55].

1. Initial analysis steps

This pipeline uses short Fourier transforms (SFTs) of the time domain $h(t)$ as its input data, with a coherent duration of each chunk varying as a function of the searched frequency (as shown in Table III). It creates peak-grams, which are spectrograms with the normalized power substituted by 1s (if the power is above a certain threshold $\rho_t = 1.6$) and 0s, where the normalized power in a frequency bin is defined as

$$\rho_k = \frac{|\tilde{x}_k^2|}{\langle n_k \rangle^2}, \tag{10}$$

TABLE III. Coherent times and number of SFTs for each frequency range searched by the *SkyHough* pipeline. The last column shows the number of SFTs per dataset, and the numbers in parentheses the SFTs used at the second step of the search.

Frequency [Hz]	T_c [s]	N_{SFT}
[50, 300)	3600	2544 (4755)
[300, 550)	2700	3460 (6568)
[550, 1300)	1800	5283 (10195)
[1300, 1500)	900	10801 (21200)

where $\langle n_k \rangle^2$ is estimated with a running median of 101 frequency bins.

We use the Hough transform to track the time-frequency evolution of the signal including the Doppler modulation of the signal at the detector. In the first stage the pipeline employs a look-up Table (LUT) approach, taking into account that at a given time the same Doppler modulation is produced by an annulus of sky positions (given by $\Delta\theta$), which correspond to the width of a frequency bin Δf:

$$\cos\Delta\theta = \frac{c}{v(t)}\frac{f(t)-\hat{f}(t)}{\hat{f}(t)} = \frac{c}{v(t)}\frac{\Delta f}{\hat{f}(t)}, \tag{11}$$

where $f(t)$ is the observed frequency at the detector and $\hat{f} = f_0 + f_1 t$ is the searched frequency. The algorithm tracks the sky positions which produce observed frequencies with powers above the threshold. It then stacks these sky positions by following the evolution of the source frequency given by the spin-down/up term at different time stamps and produces a final histogram. The LUT approach reuses the same Doppler modulation pattern for different search frequencies (more details in [42]), which produces computational savings in exchange for not following the exact frequency-time pattern.

For each template (described by f_0, $\dot{f}, \alpha, \delta$) being searched, a detection statistic called number count significance is calculated:

$$s_n = \frac{n - \langle n \rangle}{\sigma_n}, \tag{12}$$

where $\langle n \rangle$ and σ_n are the expected mean and standard deviation of the Hough number count n when only noise is present. The number count n is the weighted sum of 1s and 0s, where the weights (which are proportional to the antenna pattern functions and inversely proportional to the power spectral density) were derived in [56].

The parameter space is separated in 0.1 Hz frequency bands and in small sky-patches. A toplist is calculated for each of these regions, which has the top templates ordered by the number count significance. For the top templates, a second step is performed where instead of using the look-up Table approach the exact frequency path is tracked. At this second step the power significance is also calculated, which is defined as

$$s_P = \frac{P - \langle P \rangle}{\sigma_P}, \tag{13}$$

where instead of summing weighted 1s and 0s the weighted normalized powers given by Eq. (10) are summed. This detection statistic improves the sensitivity of *SkyHough* with a very small increase of computational cost. The best 5000 templates per sky-patch and 0.1 Hz band are passed to the second step, and only the best 1000 candidates per sky-patch and 0.1 Hz band are used for the postprocessing. Furthermore, at the second step more SFTs are used than in the first step. This is achieved by sliding the initial times of each SFT that was used at the first step, obtaining more SFTs (approximately twice the previous amount), all of them of T_c contiguous seconds.

The grid resolution was obtained in [42] and it is given by

$$\delta f = \frac{1}{T_c} \tag{14}$$

$$\delta\dot{f} = \frac{1}{T_c T_{\mathrm{obs}}} \tag{15}$$

$$\delta\theta = \frac{c}{v T_c f P_F}, \tag{16}$$

where P_F is a parameter which controls the sky resolution grid. In this search we have set $P_F = 2$ for all frequencies.

2. Postprocessing

The postprocessing consists of several steps:

(1) The output of the main SkyHough search is one toplist for each dataset (there are two datasets, each one with data from two detectors, detailed in Table V) and each region in parameter space. We search for coincidental pairs between these toplists, by calculating the distance in parameter space and selecting the pairs which are closer than a certain threshold called d_{co}. For the coincidental pairs the centers (average locations in parameter space weighted by significance) are calculated. The parameter space distance is calculated as

$$d_{SH} = \sqrt{\left(\frac{\Delta f}{\delta f}\right)^2 + \left(\frac{\Delta \dot{f}}{\delta \dot{f}}\right)^2 + \left(\frac{\Delta x}{\delta x}\right)^2 + \left(\frac{\Delta y}{\delta y}\right)^2}, \tag{17}$$

where the numbers in the numerators represent the difference between to templates and the numbers in the denominators represent the parameter resolution (this distance is unitless and is given as a number of bins). The parameters x and y are the Cartesian ecliptic coordinates projected in the ecliptic plane.

(2) Search for clusters in the obtained list of centers. This will group different outliers which can be ascribed to a unique physical cause, and will reduce

the size of the final toplist. Again, we set a threshold in parameter space distance (called $d_{\rm cl}$) and we find candidates which are closer than this distance.

(3) Finally, we calculate the centers of the clusters. This is done as a weighted (by significance) average, taking into account all the members of the cluster. We order the obtained clusters in each 0.1 Hz by their sum of the power significance of all the members of a cluster, and we select the highest ranked cluster per 0.1 Hz band, if any. This produces the final list of clusters with their parameters (f_0, $\dot{f}, \alpha, \delta$) which will be the outliers to be followed up.

3. Follow-up

We describe a follow-up method based on the $\mathcal{F}$-statistic (described in more detail in Sec. IV C) and the GCT metric method [57]. This method uses the *lalapps_HierarchSearchGCT* code, part of the publicly available LALSuite [55], and it is similar in spirit to the multistep follow-up methods described in [58] or [59].

The goal is to compare the $\mathcal{F}$-statistic values obtained from software injected signals to the $\mathcal{F}$-statistic values obtained from the outliers. We want to compare the $\mathcal{F}$-statistic obtained at different stages which scale the coherent time. It is expected that for an astrophysical signal the $\mathcal{F}$-statistic value should increase if the coherent time increases.

The resolution in parameter space is given by [57]

$$\delta f = \frac{\sqrt{12m}}{\pi T_c} \tag{18}$$

$$\delta \dot{f} = \frac{\sqrt{720m}}{\pi T_c^2 \gamma} \tag{19}$$

$$\delta\theta = \frac{\sqrt{m_{\rm sky}}}{\pi f \tau_e}, \tag{20}$$

where m and $m_{\rm sky}$ are mismatch parameters, γ is a parameter which gives the refinement between the coherent and semicoherent stages and $\tau_e = 0.021$ s represents the light time travel from the detector to the center of the Earth.

We now enumerate the different steps of the procedure:

(1) Calculate the semicoherent $\mathcal{F}$-statistic of outliers with $T_c = 7200$ s in a cluster box.

(2) Add injections to the original data using a sensitivity depth ($\sqrt{S_n}/h_0$) value which returns $\mathcal{F}$-statistic values similar to the values obtained with the outliers in order to compare similar signals. We inject signals in eight different frequency bands with 200 injections per band, with a sensitivity depth of 42 $\mathrm{Hz}^{-1/2}$. Then, search in a small region (around ten bins in each dimension) around the true parameters of the injections with $T_c = 7200$ s. Finally, analyze the distances in parameter space from the top candidates to the injections.

TABLE IV. Coherent times and mismatch parameters at each different stage of the *SkyHough* follow-up.

Stage index	T_c [s]	m	$m_{\rm sky}$
I	7200	0.1	0.01
II	72 000	0.1	0.003
III	720 000	0.1	0.0005

(3) Repeat the previous step increasing the coherent time to $T_c = 72000$ s.

(4) Calculate $\mathcal{F}_{72000\ \rm s}/\mathcal{F}_{7200\ \rm s}$ for each of the 1600 injections using the top candidates. The threshold will be the minimum value.

(5) Calculate the $\mathcal{F}$-statistic values of outliers with $T_c = 72000$ s around the top candidate from the first stage. The size of the window to be searched is estimated from the distances found in step 2.

(6) Calculate $\mathcal{F}_{72000\ \rm s}/\mathcal{F}_{7200\ \rm s}$ using the top candidate for all outliers. Outliers with values higher than the threshold obtained in step 4 go to the next comparison, and the process is repeated from step 2 increasing the coherent time.

Table IV summarizes the parameters that we have chosen at each different stage. As we will see in the Results section, only two comparisons between three different stages were needed.

C. Time-domain $\mathcal{F}$-statistic

The *Time-domain $\mathcal{F}$-statistic* search method uses the algorithms described in [33,43,60,61] and has been applied to an all-sky search of VSR1 data [33] and an all-sky search of the LIGO O1 data [38,40]. The main tool is the $\mathcal{F}$-statistic [43] by which one can search coherently the data over a reduced parameter space consisting of signal frequency, its derivatives, and the sky position of the source. The $\mathcal{F}$-statistic eliminates the need for a grid search over remaining parameters [see Eqs. (1) and (4)], in particular, the inclination angle ι and polarization ψ. Once a signal is identified the estimates of those four parameters are obtained from analytic formulas.

However, a coherent search over the whole LIGO O2 dataset is computationally prohibitive and we need to apply a semicoherent method, which consists of dividing the data into shorter time domain segments. The short time domain data are analyzed coherently with the $\mathcal{F}$-statistic. Then the output from the coherent search from time domain segments is analyzed by a different, computationally manageable method. Moreover, to reduce the computer memory required to do the search, the data are divided into narrow-band segments that are analyzed separately. Thus our search method consists primarily of two parts. The first part is the coherent search of narrow-band, time-domain segments. The second part is the search for coincidences among the candidates obtained from the coherent search.

The pipeline is described in Sec. IV of [38] (see also Fig. 13 of [38] for the flow chart of the pipeline). The same pipeline is used for the search of LIGO O2 data presented here except that a number of parameters of the search are different. The choice of parameters was motivated by the requirement to make the search computationally manageable.

As in our O1 searches, the data are divided into overlapping frequency subbands of 0.25 Hz. We analyze three frequency bands: [20–100], [100–434], and [1518–1922] Hz. As a result, the three bands have 332, 1379, and 1669 frequency subbands respectively.

The time series is divided into segments, called frames, of 24 sidereal days long each, six days long, and two days long respectively for the three bands. Consequently in each band we have 11, 44, and 134 time frames, respectively. The O2 data has a number of nonscience data segments. The values of these bad data are set to zero. For this analysis, we choose only segments that have a fraction of bad data less than $1/2$ both in H1 and L1 data. This requirement results in eight 24-day-long, twenty-six six-day-long, seventy-nine two-day-long data segments for each band respectively. These segments are analyzed coherently using the $\mathcal{F}$-statistic defined by Eq. (9) of [33]. We set a fixed threshold for the $\mathcal{F}$-statistic of $\mathcal{F}_0 = 16$ and record the parameters of all threshold crossings, together with the corresponding values of the signal-to-noise ratio ρ,

$$\rho = \sqrt{2(\mathcal{F} - 2)}. \tag{21}$$

Parameters of the threshold crossing constitute a candidate signal. At this first stage we also veto candidate signals overlapping with the instrumental lines identified by independent analysis of the detector data.

For the search we use a four-dimensional grid of templates (parametrized by frequency, spin-down/up, and two more parameters related to the position of the source in the sky) constructed in Sec. IV of [61]. For the low frequency band [20–434] Hz we choose the grid's minimal match MM $= \sqrt{3}/2$ whereas for the high frequency band [1518–1922] Hz we choose a looser grid with MM $= 1/2$.

In the second stage of the analysis we search for coincidences among the candidates obtained in the coherent part of the analysis. We use exactly the same coincidence search algorithm as in the analysis of VSR1 data and described in detail in Sec. VIII of [33]. We search for coincidences in each of the subbands analyzed. To estimate the significance of a given coincidence, we use the formula for the false alarm probability derived in the Appendix of [33]. Sufficiently significant coincidences are called outliers and subjected to further investigation.

The sensitivity of the search is estimated by the same procedure as in O1 data analysis ([38], Sec. IV). The sensitivity is taken to be the amplitude h_0 of the gravitational wave signal that can be confidently detected. We perform the following Monte Carlo simulations. For a given amplitude h_0, we randomly select the other seven parameters of the signal: $f, \dot{f}, \alpha, \delta, \phi_0, \iota$ and ψ. We choose frequency and spin-down/up parameters uniformly over their range, and source positions uniformly over the sky. We choose angles ϕ_0 and ψ uniformly over the interval $[0, 2\pi]$ and $\cos\iota$ uniformly over the interval $[-1, 1]$. We add the signal with selected parameters to the O1 data. Then the data are processed through our pipeline. First, we perform a coherent $\mathcal{F}$-statistic search of each of the data segments where the signal was added. Then the coincidence analysis of the candidates is performed. The signal is considered to be detected, if it is coincident in more than five of the eight time frames analyzed, 14 out of 26, and 40 out of 79 for the three bands respectively. We repeat the simulations 100 times. The ratio of numbers of cases in which the signal is detected to the 100 simulations performed for a given h_0 determines the frequentist sensitivity upper limits. We determine the sensitivity of the search in each 0.25 Hz frequency subband separately. The 95% confidence upper limits for the whole range of frequencies are given in Fig. 12; they follow very well the noise curves of the O2 data that were analyzed. The sensitivity of search decreases with decreasing coherence time we use for the three bands of our $\mathcal{F}$-statistic search. Additionally it decreases in our high-frequency band because of the looser grid used than in low frequency bands.

V. RESULTS

In this section we detail the results obtained. The region in frequency and first frequency derivative searched by each of the three different pipelines is shown in Fig. 2.

Although no detections have been made, we give details on the different procedures and outliers which were found, and we also present 95% confidence level (C.L.) upper limits on the strain h_0 given by Eq. (2), shown in Fig. 3.

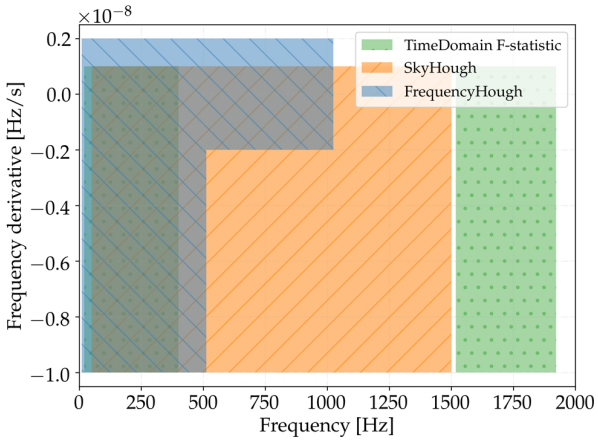

FIG. 2. Regions in frequency and first frequency derivative covered by each pipeline.

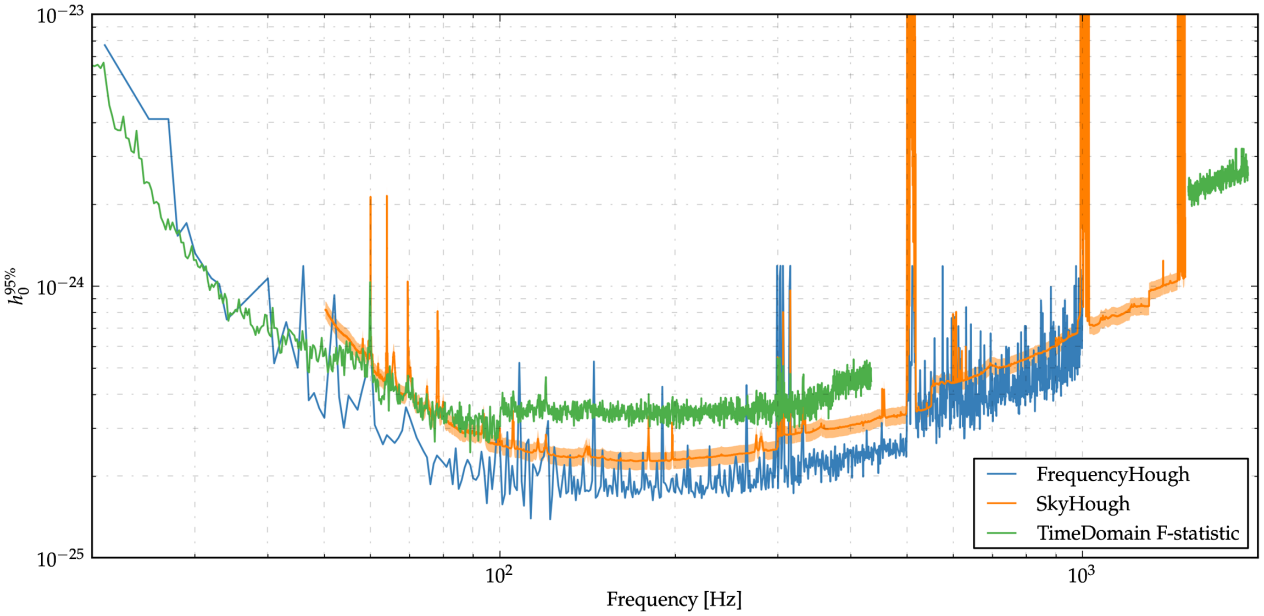

FIG. 3. Upper limits on the strain amplitude $h_0^{95\%}$ for the three pipelines.

The best upper limit is $\simeq 1.7 \times 10^{-25}$ at around 120 Hz. These results are significantly better (of a factor of about 1.4) than those obtained on O1 data with the same pipelines [38,40], thanks to improvements in the pipelines themselves, to the better sensitivity of the detectors and to the longer duration of the observing run. These upper limits do not take into account the calibration uncertainty on amplitude, which over the run was no larger than 5% and 10% for H1 and L1 respectively [48].

Our O2 results are comparable with the upper limits obtained in O1 by the Einstein@Home project [39] over the range 20–100 Hz. Note, however, that the Einstein@Home search covered a spin-down/up range smaller by almost 1 order of magnitude. Moreover, while the Einstein@Home search is, in principle, more sensitive due to the use of much longer data segments (compared to the *FrequencyHough* and *SkyHough* pipelines), with 210 hr duration, it is also less robust in case of deviations from the assumed signal model described in Sec. III. At frequencies higher than 100 Hz, the previous best upper limits were obtained in [62] using O1 data. Our results improve on those upper limits by approximately 17%.

The 95% C.L. upper limits on h_0 can be converted to upper limits on ellipticity ϵ by using Eq. (2) with a canonical value for the moment of inertia of 10^{38} kg m^2 and by using different distances:

$$\epsilon = \frac{c^4}{4\pi^2 G}\frac{h_0 d}{I_{zz} f^2}. \tag{22}$$

These results are shown in the left panel of Fig. 4. This has been obtained by using the best h_0 upper limits between the three pipelines: from 20 to 1000 Hz, the *FrequencyHough* results have been used; from 1000 to 1500 Hz, the results from *SkyHough* have been used; from 1518 to 1922 Hz the results from *Time-domain $\mathcal{F}$-statistic* have been used. For sources at 1 kpc emitting CWs at 500 Hz, we can constrain the ellipticity at $\simeq 10^{-6}$, while for sources at 10 kpc emitting at the same frequency we can constrain the ellipticity at 10^{-5}.

A complementary way of interpreting the limits on ellipticity is shown in the right panel of Fig. 4. The various set of points give the relation between the absolute value of the signal frequency time derivative (spin-down) and the signal frequency for sources detectable at various distances, assuming their spin-down is only due to the emission of gravitational waves. They have been computed by means of the following relation obtained inverting the equation for the so-called spin-down limit amplitude h_0^{sd}, which is a function of the source distance d, frequency f and spin-down $\dot{f}$, see e.g., Eq. (A7) in [63]:

$$|\dot{f}| = 1.54 \times 10^{-10} \left(\frac{I_{zz}}{10^{38}\ \mathrm{kg\,m^2}}\right)^{-1} \left(\frac{h_0^{\mathrm{sd}}}{10^{-24}}\right) \times \left(\frac{f}{100\ \mathrm{Hz}}\right) \left(\frac{d}{1\ \mathrm{kpc}}\right)^2 \ [\mathrm{Hz/s}], \tag{23}$$

where we have replaced the spin-down limit amplitude with the 95% upper limits shown in Fig. 3. The dashed lines are constant ellipticity curves obtained from Eq. (A9) of [63]:

$$|\dot{f}| = 1.72 \times 10^{-14} \left(\frac{I_{zz}}{10^{38}\ \mathrm{kg\,m^2}}\right) \left(\frac{f}{100\ \mathrm{Hz}}\right)^{1/2} \times \left(\frac{\varepsilon}{10^{-6}}\right)^2 \ [\mathrm{Hz/s}]. \tag{24}$$

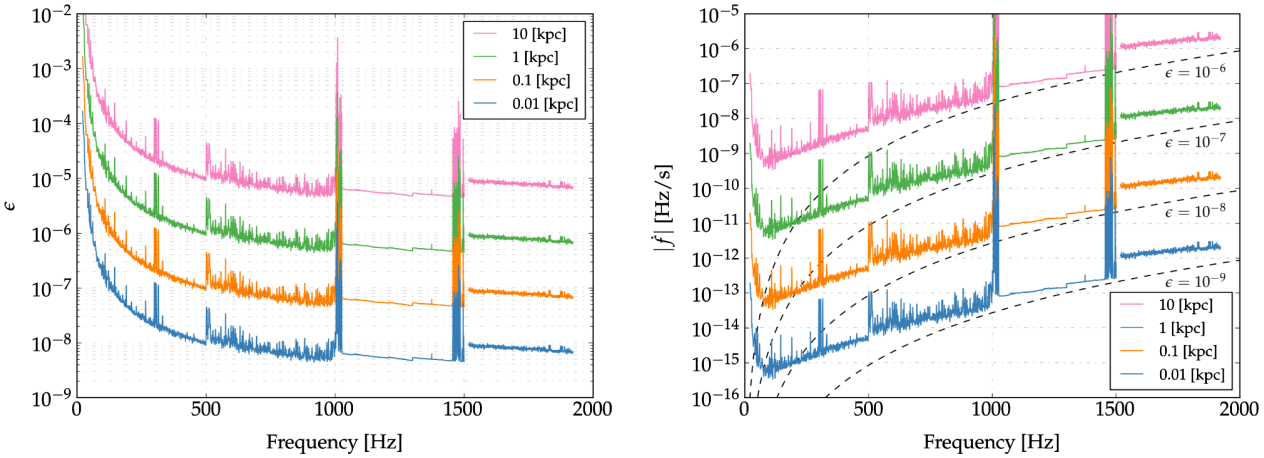

FIG. 4. The left panel shows the detectable ellipticity given by Eq. (22) as a function of frequency for neutron stars at 10 pc, 100 pc, 1 kpc and 10 kpc for a canonical moment of inertia $I_{zz} = 10^{38}$ kg m^2. The right panel shows the relation between the absolute value of the first frequency derivative and the frequency of detectable sources as a function of the distance, assuming their spin-down is due solely to the emission of gravitational waves. The different colors correspond to the same distances of the left panel. Black dashed lines are lines of constant source ellipticity, from $\varepsilon = 10^{-9}$ (bottom dashed line) to $\varepsilon = 10^{-6}$.

For a signal to be detectable, its spin-down/up would need to be equal or above the given traces (notice that, as shown in Fig. 2, the maximum absolute spin-down searched is 10^{-8} Hz/s, which marks a limit to the signals we are sensitive to). For example, a source emitting a signal with frequency higher than about 500 Hz and ellipticity equal or greater than 10^{-6} would be detectable up to a distance of about 1 kpc if its spin-down is, in modulus, larger than $\approx 10^{-10}$ Hz/s.

The three searches carried out by the different pipelines have different computational costs: *FrequencyHough* spent 9 MSU; *SkyHough* spent 2.5 MSU; *Time-domain $\mathcal{F}$-statistic* spent 24.2 MSU, where 1 MSU hour corresponds to 1 million Intel E5-2670 core-hour to perform a SPECfp computation. We remind the reader that each of these pipelines covered different search bands.

A. FrequencyHough

In this section we report the main results of the O2 all-sky search using the *FrequencyHough* pipeline. The spin-down range covered by the analysis is $(+2 \times 10^{-9}$ Hz/s, -10^{-8} Hz/s) up to 512 Hz and $(+2 \times 10^{-9}$ Hz/s, -2×10^{-9} Hz/s) from 512 Hz up to 1024 Hz.

The number of initial candidates produced by the *FrequencyHough* transform stage was about 5×10^9 (of which about 7×10^7 belong to the band 20–128 Hz, about 1.1×10^9 to the band 128–512 Hz and about 3.8×10^9 to the band 512–1024 Hz, for both Hanford and Livingston detectors. As the total number of coincident candidates remained too large, 1.09×10^8, we reduced it with the ranking procedure described in Sec. IV A. The total number of candidates selected after the ranking was 59025. Each of these candidates was subject to a multistage follow-up procedure, described in Sec. IV A 2. The total number of candidates passing the follow-up and all the veto steps was 154, after removing the candidates due to the hardware injections. Among these, only 27 were found in coincidence between the two detectors [within a distance $d_{\mathrm{FH}} < 3$ as defined in (9)]. From these surviving candidates we selected the outliers less consistent with noise fluctuations. In particular, we choose those for which the final peakmap projections have an average (over the two detectors) critical ratio (see Sec. IV A 2) CR > 7.42. This is the threshold corresponding, under the assumption of Gaussian noise, to a false alarm probability of 1% after having taken into account the look-elsewhere effect (on the follow-up stage) [38]. We found only one candidate an average CR above the threshold. It was at a frequency of about 440.4 Hz, and occurred due to a high CR value in the LIGO Hanford detector. For this candidate, we have looked at the starting peakmaps, without Doppler correction, around its frequency, which clearly show the presence of a transient line of duration ≈ 2 days at the candidate frequency in Hanford data, see Fig. 5. We have then discarded this candidate as a possible CW signal. The remaining 26 subthreshold candidates, which will be further analyzed in a forthcoming work, are listed in VI. The analysis was run on distributed computational resources accessed through the EGI grid middleware [64].

As we did not find any significant candidate, we have computed upper limits. They have been evaluated in 1-Hz bands, as described in IV A 3, and are shown in Fig. 3. The total amount of frequency bands vetoed by the persistency veto is negligible, as it amounts to less than 0.55% and 0.45% respectively for LIGO Hanford and Livingston. There are a few 1 Hz bands where we have not evaluated the upper limit, due to the fact that we do not have

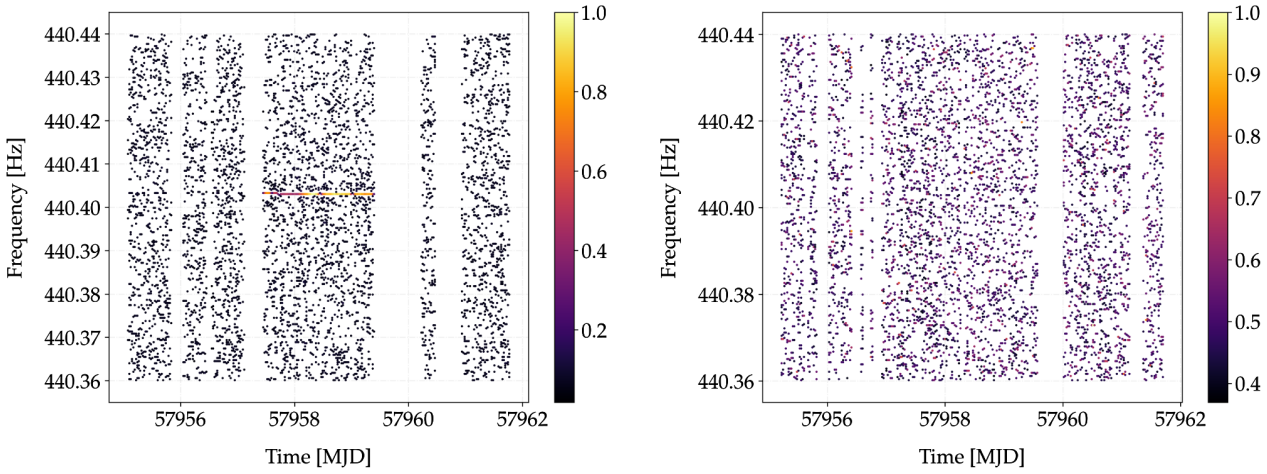

FIG. 5. *FrequencyHough* peakmaps, without Doppler correction, around the outlier at ∼440.4 Hz, for Hanford (left) and Livingston (right) data. The presence of a transient line is clearly visible in Hanford. The x-axis indicates time in modified Julian date (MJD).

candidates or, due to disturbances, we have not been able to recover the 95% of the injections, or more, at any amplitude. These bands are those with the following initial frequencies: $\{22, 23, 24, 26, 35, 36, 37, 39, 42, 51, 56, 65, 71, 73, 79, 120, 763, 995, 996, 998\}$ Hz. Comparing upper limits with O1 results [38], see Fig. 6, we notice an improvement of ∼30%–40% at frequencies between ∼150 and 500 Hz, while the gain is significantly bigger, up to a factor of ∼2, at lower frequencies. This is the first time we have extended the *FrequencyHough* analysis above ∼500 Hz. The statistical uncertainty on the upper limit is lower than about 5%, because of the amplitude step used for the injections, which amounts to 2×10^{-26}.

As a test of the capabilities of the pipeline to recover signals, we report in Appendix A 1 the parameters of the recovered hardware injections, together with the error with respect to the injected signals. We note that we were able to recover, with very good accuracy, the parameters of all 12 hardware injections with frequency in the analyzed band.

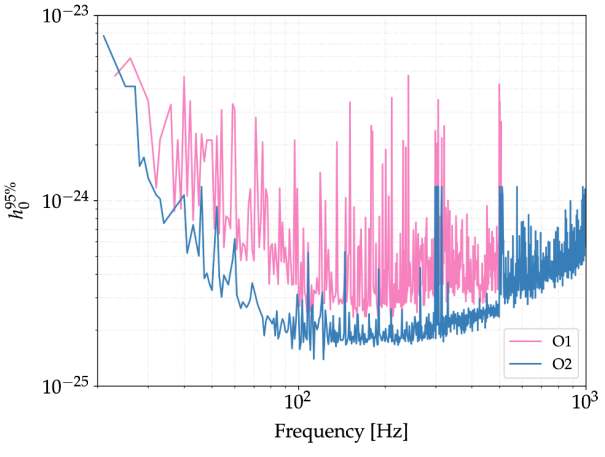

FIG. 6. Comparison of O1 and O2 95% upper limits on the strain amplitude for the *FrequencyHough* pipeline. The O2 search covered the range between 20 and 1000 Hz, while the O1 search arrived up to 475 Hz. They have been obtained adding simulated signals to the real data, covering the same parameter space as in the actual search.

B. SkyHough

SkyHough has analyzed frequencies from 50 to 1500 Hz and spin-down/up values from -10^{-8} to 10^{-9} Hz/s as shown in Fig. 2. The four different coherent times that have been used are shown in Table III. This analysis uses the C02 cleaned dataset [48], and splits the data from H1 and L1 in two datasets, divided by time as shown in Table V, where the start and stop times for each dataset are indicated. The main search generates a toplist per dataset per 0.1 Hz band of 10000 candidates with a maximum of 1000 per sky-patch. The number of sky-patches depends on the frequency: to minimize the computational cost of the search, we try to minimize the number of sky-patches for a limited amount of random access memory. From 50 to 850 Hz, there are 28 sky-patches; from 850 to 1000 Hz, 31 sky-patches; from 1000 to 1150 Hz, 38 sky-patches; from 1150 to 1250 Hz, 45 sky-patches; from 1300 to 1500 Hz, 28 sky-patches. After applying the postprocessing stage previously described (with distance thresholds of $d_{\mathrm{co}} = 3$ and $d_{\mathrm{cl}} = \sqrt{14}$), we are left with 4548 0.1 Hz bands (from a total of 14500) having coincidental pairs.

TABLE V. Start/stop times in GPS units of each dataset used by the *SkyHough* pipeline. The observation time parameter used for the spin-down resolution given by Eq. (16) is $T_{\mathrm{obs}} = 7915032$ s, the maximum span of these datasets.

Dataset 1	H1	1167545839/1174691692
	L1	1167546403/1174688389
Dataset 2	H1	1180982628/1187731792
	L1	1179816663/1187731695

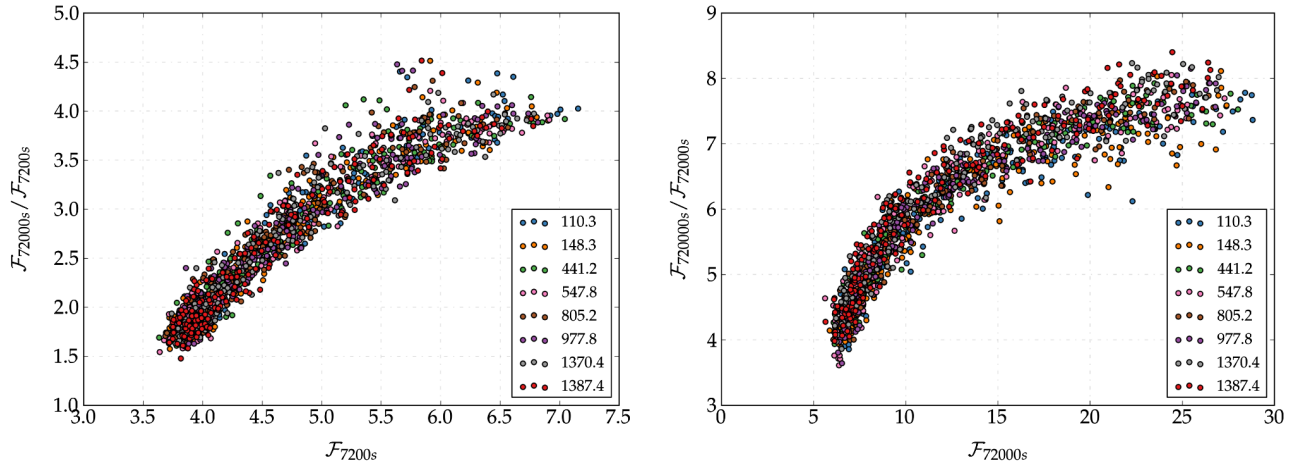

FIG. 7. Results from software injections for the first (left panel) and second (right panel) comparisons between the first and last two stages of Table IV of the *SkyHough* follow-up. The vertical axis shows the quotient between the top candidates at the two stages, and the horizontal axis shows the values of the top candidates at the stage with lowest T_c. The lowest points, equal to 1.47 and 3.66 respectively, set the thresholds for the follow-up veto. Each color represents a different frequency band.

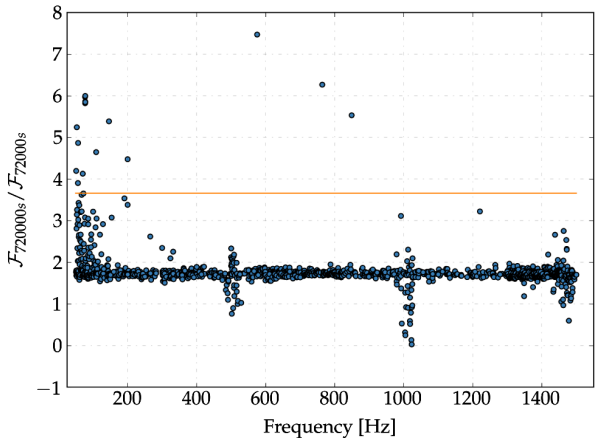

FIG. 8. Results of the second follow-up comparison (using stages II and III) for the *SkyHough* outliers. Only 17 outliers are above the threshold. The horizontal line marks the threshold at 3.66, which was obtained in Sec. IV B 3.

We apply the *population veto*, used in many past searches, which demands that each dataset contributes to each cluster with at least two different templates. After applying this veto, only 1539 outliers remain.

The next step is to apply the $\mathcal{F}$-statistic follow-up method described in Sec. IV B 3 to these 1539 outliers. The thresholds obtained are 1.47 and 3.66 for the first and second comparison respectively, as shown in Fig. 7. Only 17 outliers are above the threshold at 3.66, as shown in Fig. 8. All of the outliers which are above the final threshold correspond to one of the hardware injections listed in Table VII or to one known source of instrumental noise, listed in [46]. The 17 surviving outliers and their parameters are listed in Table VIII, with comments about their likely origin.

We recover six of the nine hardware injections that are in the *SkyHough* searched parameter space. We lose the other three mainly for two reasons: there were brief periods when the hardware injections were not active, which causes the increase of the $\mathcal{F}$-statistic to not be as high as it should be (this happens to two of the three lost hardware injections, which are present in our initial list of 1539 outliers); we only select one cluster per 0.1 Hz band, and if in that band there is a more significant cluster due to a noise disturbance the signal cluster will not be followed (this happens to one of the three lost hardware injections, which forms a cluster but a more significant noise disturbance is present in that 0.1 Hz band).

TABLE VI. The second column shows the frequency bands used to estimate the *SkyHough* upper limits on gravitational-wave signal amplitude h_0. The third column shows the injected sensitivity depth values given by Eq. (25), and the last column shows the sensitivity depth at 95% confidence for each group.

T_c [s]	Frequency [Hz]	Injected $\mathcal{D}$ [$1/\mathrm{Hz}^{-1/2}$]	$\mathcal{D}^{95\%}$ [$1/\mathrm{Hz}^{-1/2}$]
3600	110.3, 136.1, 148.3, 165.6, 182.6, 206.1, 225.6, 241.5, 261.3, 286.7	27.5, 28.5, 29.5, 30.5, 31.5	32.4
2700	311.6, 325.4, 342.5, 363.3, 394.0, 412.4, 432.8, 441.2, 523.4, 547.8	26.5, 27.5, 28.5, 29.5, 30.5	29.2
1800	594.6, 661.1, 741.4, 805.0, 866.2, 933.1, 977.6, 1064.7, 1141.5, 1250.7	23.0, 24.0, 25.0, 26.0, 27.0	25.2
900	1313.4, 1331.7, 1358.4, 1370.3, 1388.8, 1402.4, 1423.1, 1430.3, 1443.4, 1464.6	22.0, 23.0 24.0, 25.0, 26.0	22.3

TABLE VII. Parameters of the hardware-injected simulated continuous-wave signals during the O2 data run (parameters given at epoch GPS 1130529362).

Label	Frequency [Hz]	Spin-down [nHz/s]	α [deg]	δ [deg]
ip0	265.575533	-4.15×10^{-3}	71.55193	−56.21749
ip1	848.969641	-3.00×10^{-1}	37.39385	−29.45246
ip2	575.163521	-1.37×10^{-4}	215.25617	3.44399
ip3	108.857159	-1.46×10^{-8}	178.37257	−33.4366
ip4	1393.540559	-2.54×10^{-1}	279.98768	−12.4666
ip5	52.808324	-4.03×10^{-9}	302.62664	−83.83914
ip6	146.169370	-6.73×10^{0}	358.75095	−65.42262
ip7	1220.555270	-1.12×10^{0}	223.42562	−20.45063
ip8	191.031272	-8.65×10^{0}	351.38958	−33.41852
ip9	763.847316	-1.45×10^{-8}	198.88558	75.68959
ip10	26.341917	-8.50×10^{-2}	221.55565	42.87730
ip11	31.424758	-5.07×10^{-4}	285.09733	−58.27209
ip12	38.477939	-6.25×10^{0}	331.85267	−16.97288
ip13	12.428001	-1.00×10^{-2}	14.32394	−14.32394
ip14	1991.092401	-1.00×10^{-3}	300.80284	−14.32394

Although no detections were made, we produce all-sky averaged upper limits on the strain of the signal h_0 (these upper limits are valid for all the frequency bands except the ones which have one of the 1539 outliers). We add software simulated signals to the original data by using *lalapps_Makefakedata_v5*. We have injected signals at ten different 0.1 Hz bands for each of the four coherent times (a total of 40 bands), which can be seen in Table VI. These are bands which do not have outliers or instrumental known sources of lines or combs.

We have used five different sensitivity depths at each coherent time, with 400 signals per sensitivity depth. The sensitivity depth is given by

$$\mathcal{D} = \frac{\sqrt{S_n}}{h_0}, \tag{25}$$

where S_n is the one-sided power spectral density. We inject signals at random positions in the sky, covering the full spin-down/up range and with random polarization, inclination and initial phase. For each band and depth, we calculate the efficiency (number of detected signals divided by total number of signals). We follow the same procedure as in the all-sky search: we run the main search and then apply coincidences, clustering and the population veto. We assume that a signal is detected if the total distance from the recovered cluster to the actual injection is less than 13 bins.

At each of the 40 frequency bands, we fit a sigmoid given by

$$s = 1 - \frac{1}{1 + e^{b(x-a)}}. \tag{26}$$

An example of this fitting can be seen in Fig. 9. From the estimated coefficients a and b along with the covariance

TABLE VIII. 17 outliers from the *SkyHough* pipeline which survived the follow-up procedure. All of them can be ascribed to a hardware injection or to a known source of instrumental noise. The $(f_0, \dot{f}, \alpha, \delta)$ values correspond to the center of the cluster returned by the postprocessing stage. The $\bar{s}_P$ column shows the mean power significance of the cluster, while the $\mathcal{F}$ column shows the $\mathcal{F}$-statistic mean over segments of the top candidate obtained at the last stage of the follow-up. The reference time for these parameters is 1167545839 GPS.

Outlier index	Frequency [Hz]	Spin-down [nHz/s]	α [deg]	δ [deg]	Population	$\bar{s}_P$	$\mathcal{F}$	Description
7	51.0002	-1.8346×10^{-11}	87.0087	−66.0873	6542	50.16	86.0406	1 Hz comb at H1 and L1
18	52.8083	2.2838×10^{-12}	299.6708	−83.3562	1433	124.12	654.9832	Hardware injection 5
36	56.0001	-6.3195×10^{-12}	88.8156	−66.4443	2765	210.17	157.7912	1 Hz comb at H1 and L1
39	56.4957	5.7155×10^{-10}	156.8932	−49.1672	111	9.04	72.64532	1 Hz comb at H1 and L1
113	70.0001	-1.2045×10^{-11}	88.1699	−66.1180	2980	121.85	165.2225	1 Hz comb at H1 and L1
125	72.0001	-5.4952×10^{-12}	89.4121	−66.5021	3471	57.69	64.56955	1 Hz comb at H1 and L1
149	76.6788	-1.7870×10^{-10}	74.5911	−59.0142	397	32.66	444.1439	0.08843966 Hz comb at H1
150	76.9442	-1.8308×10^{-10}	74.6723	−58.9216	558	36.12	566.2429	0.08843966 Hz comb at H1
151	77.1207	-1.4130×10^{-10}	77.8483	−59.1510	129	26.81	507.6696	0.08843966 Hz comb at H1
152	77.2090	-1.3071×10^{-10}	79.0815	−59.5503	93	21.51	405.0106	0.08843966 Hz comb at H1
153	77.3855	-7.9419×10^{-11}	279.3909	70.9090	150	14.78	154.7181	Unknown line at H1
316	108.8567	4.3434×10^{-11}	182.2717	−29.6472	3050	72.87	275.9235	Hardware injection 3
485	145.9203	-6.7301×10^{-9}	358.7866	−65.2887	675	86.45	311.7228	Hardware injection 6
664	199.9977	-1.5070×10^{-11}	89.5203	−66.2582	1249	83.46	130.1102	99.9987 Hz comb at H1
1629	575.1638	-2.9038×10^{-11}	215.4209	4.0846	636	564.51	4962.3050	Hardware injection 2
2303	763.8471	1.2199×10^{-11}	198.9249	75.6197	1798	637.28	2703.2552	Hardware injection 9
2584	848.9591	-3.4856×10^{-10}	37.3061	−28.8880	443	898.46	4473.9817	Hardware injection 1

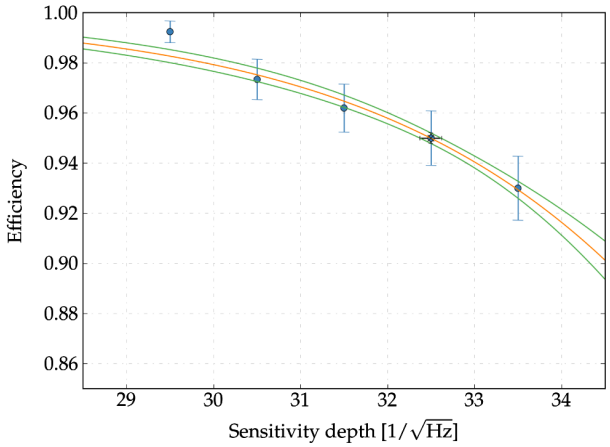

FIG. 9. Efficiency as a function of sensitivity depth and fitting at 148.3 Hz for the *SkyHough* pipeline. The vertical error bars for the blue points show the 1-sigma binomial error. The 95% efficiency point (indicated with a black cross) also shows a 1-sigma error bar, calculated with Eq. (27).

matrix C_{ab}, we calculate the 1-sigma envelope (the error) on the fit, which is given by

$$\sigma_S = \pm\sqrt{\left(\frac{\delta s}{\delta a}\right)^2 C_{aa} + \left(\frac{\delta s}{\delta b}\right)^2 C_{bb} + 2\frac{\delta s}{\delta a}\frac{\delta s}{\delta b}C_{ab}}. \quad (27)$$

After finding the 95% efficiency sensitivity depth at each of the 40 frequency bands (which can be seen in Fig. 10), we calculate a mean sensitivity depth for each of the four different frequency regions. The results are given in Table VI. From these results and by using Eq. (25), we calculate the upper limits on h_0, which are shown in Fig. 11. The trace has a shadow enclosing a 7.5% error, which we obtain by estimating the maximum difference in

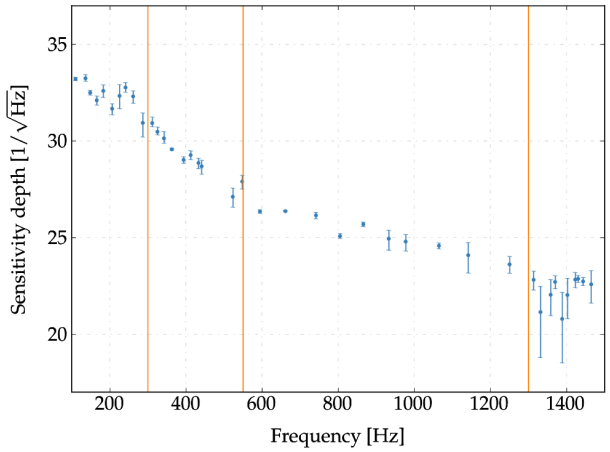

FIG. 10. The 95% sensitivity depths at each of the 40 frequency bands, with a 1-sigma error bar, for the *SkyHough* pipeline. The three vertical lines separate the four regions with different coherent time (3600, 2700, 1800, and 900 s).

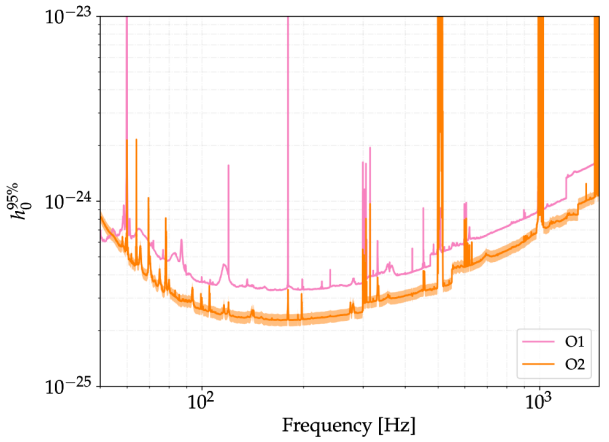

FIG. 11. 95% upper limits on h_0 for the *SkyHough* pipeline. The orange trace shows the results for the O2 search, with a shadow enclosing a 7.5% error obtained from Fig. 10, while the pink trace shows the results obtained in the O1 search. These results are valid for all frequency bands except the 1539 bands where one outlier is present.

each of the four frequency regions shown in Fig. 10 between the ten different points and the mean sensitivity depth. Figure 11 also shows a comparison with the results obtained in the previous search with O1 data.

C. Time-domain $\mathcal{F}$-statistic results

In the [20–100], [100–434], and [1518–1922] Hz bandwidth ranges under study, 3380 0.25-Hz wide subbands in total were analyzed. As a result of vetoing candidates around the known interference lines, a certain fraction of the bandwidth was not analyzed. As a result 16.0% of the band under study was vetoed.

In Figs. 13–15 the results of the coincidence search are presented for bandwidth ranges [20–100], [100–434], and [1518–1922] Hz respectively. The top panels show the maximum coincidence multiplicity for each of the subbands analyzed. The maximum multiplicity is an integer

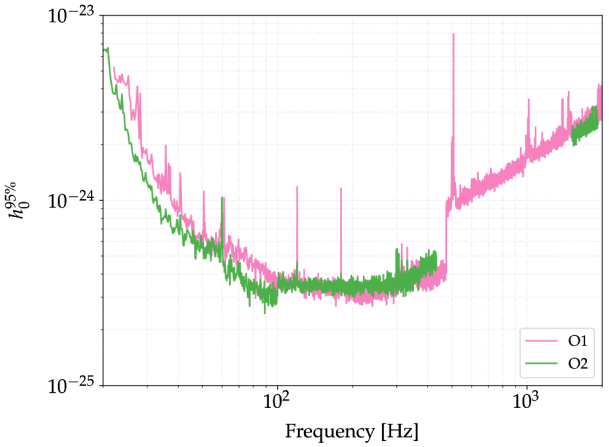

FIG. 12. Comparison of O1 and O2 95% upper limits on h_o for the *Time-domain $\mathcal{F}$-statistic* pipeline.

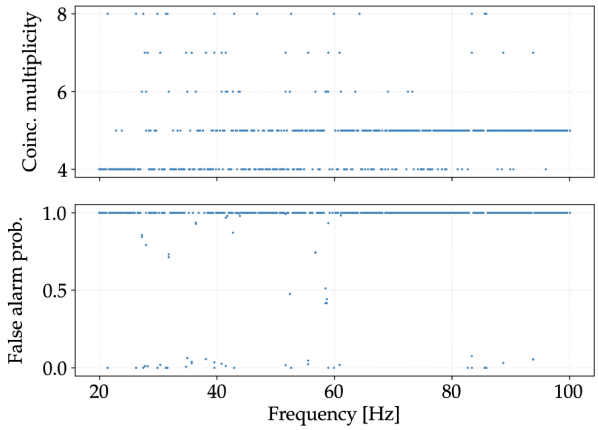

FIG. 13. Results of *Time-domain $\mathcal{F}$-statistic* pipeline coincidences as for frequency band of [20–100] Hz. Top panel: maximum coincidence multiplicity. Bottom panel: false alarm probability for the coincidence with the maximum multiplicity.

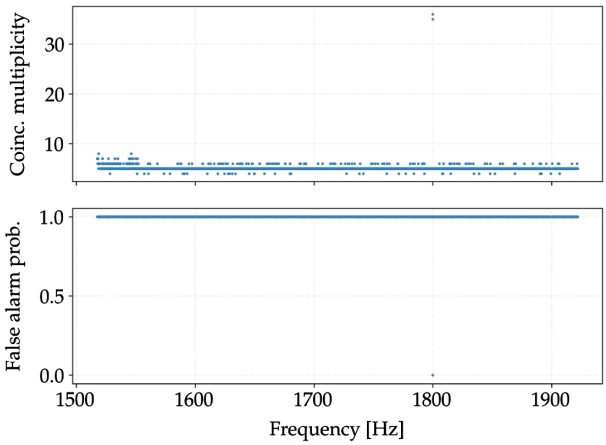

FIG. 15. Results of *Time-domain $\mathcal{F}$-statistic* pipeline coincidences as for frequency band of [1518–1922] Hz. Top panel: maximum coincidence multiplicity. Bottom panel: false alarm probability for the coincidence with the maximum multiplicity.

that varies from 4 to the number of time frames in each of the bandwidth analyzed. This is because we record coincidences of multiplicity of at least 4.

The bottom panel of Figs. 13–15 shows the results for the false alarm probability of coincidence for the coincidence with the maximum multiplicity. This is the probability that a coincidence among candidates from all the time-domain segments in a given frequency subband occurs by chance. This false alarm probability is calculated using formula (A. 6) in the Appendix of [33].

We define outliers as those coincidences with false alarm probabilities less than 0.1%. This criterion was adopted in our Virgo data search [33] and also in one of the Einstein@Home searches [28]. As a result we obtained 30 outliers. Among the 30 outliers, eight are identified with the hardware injections. Table XII presents the estimated parameters obtained for these hardware injections, along with the absolute errors of the reconstructed parameters (the differences with respect to the injected parameters).

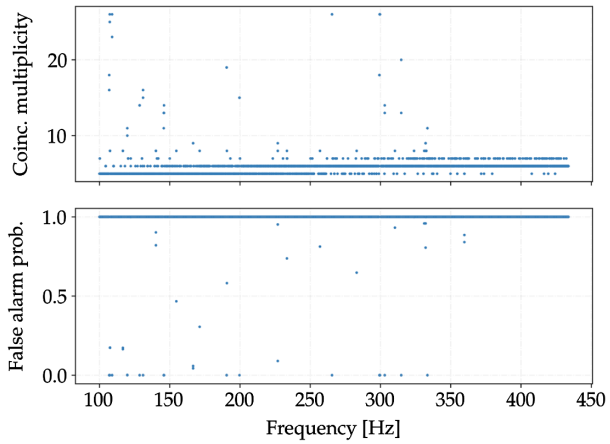

FIG. 14. Results of *Time-domain $\mathcal{F}$-statistic* pipeline coincidences as for frequency band of [100–434] Hz. Top panel: maximum coincidence multiplicity. Bottom panel: false alarm probability for the coincidence with the maximum multiplicity.

The remaining 23 outliers are listed in Table XI. They include 16 that are seen only in H1 data and three in only the L1 data. In the case of the remaining outliers their amplitude is stronger in H1 than in L1 whereas the noise level in H1 is lower than in L1. Consequently no credible gravitational wave candidates were found.

VI. CONCLUSIONS

In this paper we have presented the first results of an all-sky search for CW signals using Advanced LIGO O2 data with three different pipelines, covering a frequency range from 20 to 1922 Hz and a first frequency derivative from -1×10^{-8} to 2×10^{-9} Hz/s. For this broad range in parameter space, this is the most sensitive search up to 1500 Hz. Each search found many outliers which were followed up but none of them resulted in a credible astrophysical CW signal. On the contrary, they were ascribable to noise disturbances, to hardware injections, or consistent with noise fluctuations.

Although no detections have been made, we have placed interesting 95% C.L. upper limits on the gravitational wave strain amplitude h_0, the most sensitive being $\simeq 1.7 \times 10^{-25}$ in the 123–124 Hz region, as shown in Fig. 3. The improved results over the O1 search are due to the better sensitivity of the detectors, the use of a longer dataset and improvements of the pipelines. For the semicoherent methods used in this analysis, the strain sensitivity is proportional to [65–67]

$$h_0 \propto \sqrt{\frac{S_n}{T_{\mathrm{coh}}}} N^{\sim 1/4}. \tag{28}$$

For the same observing time, an improvement of 1.15 in the noise floor of both detectors translates to an expected improvement of 1.15 of the minimum detectable strain (looking at Fig. 1, we see that H1 has improved by ∼1.15, while L1 has improved less, so at most a factor of 1.15 is what we expect from the improved noise floors). To ascertain the influence of the run duration (assuming that the same coherent time has been used), we compare the different number of segments used. Comparing O1 [40] where ∼6600 segments were used by the *SkyHough* pipeline (similar numbers apply also for the other pipelines), with O2 where ∼10600 segments have been used, the expected improvement is of ∼1.12, which multiplied by 1.15 results in a ∼1.28 factor. The difference between this and the 1.4 observed improvement is due to the enhancement of the pipelines.

By converting the upper limits to an astrophysical reach, as shown in Fig. 4, we see that the searches presented in this paper provide already astrophysical interesting results. For instance, in the "bucket" region (around ≃150 Hz), we would be able to detect a CW signal from a neutron star within a distance of 100 pc if its ellipticity were at least 10^{-6}. Similarly, in the middle frequency range, around ≃500 Hz, we would be able to detect the CW signal up to a distance of 1 kpc, with $\epsilon > 10^{-6}$. Finally at higher frequencies, around ≃1500 Hz, the same signal would be detectable up to a distance of 10 kpc if $\epsilon > 10^{-6}$ and 1 kpc if $\epsilon > 10^{-7}$. Such levels of ellipticity are comparable or below the maximum value we may expect for neutron stars described by a standard equation of state [68]. Although approximately 2500 neutron stars have been observed through their electromagnetic emission, a much larger number of undiscovered neutron stars is expected to exist in our Galaxy, a small fraction of which could be nearby.

Further all-sky analyses are planned on O2 data, by extending the parameter space and looking at subthreshold candidates. The O3 observing run has started in April 2019 and will last for approximately 1 year. The full network of LIGO and Virgo detectors is being upgraded and improved, and we expect that the noise floor in O3 run will be significantly better than for O2. This, and the foreseen longer run duration, will make future searches more sensitive (if the noise floor improves by 1.5 and the run is 1.5 times longer than O2, we expect an improvement of ∼1.66 on the strain upper limits), increasing the chances of a CW detection or allowing us to place tighter constraints on the nonasymmetries of neutron stars in our Galaxy and to put constraints on the unseen neutron star population.

ACKNOWLEDGMENTS

The authors gratefully acknowledge the support of the United States National Science Foundation (NSF) for the construction and operation of the LIGO Laboratory and Advanced LIGO as well as the Science and Technology Facilities Council (STFC) of the United Kingdom, the Max-Planck-Society (MPS), and the State of Niedersachsen/Germany for support of the construction of Advanced LIGO and construction and operation of the GEO600 detector. Additional support for Advanced LIGO was provided by the Australian Research Council. The authors gratefully acknowledge the Italian Istituto Nazionale di Fisica Nucleare (INFN), the French Centre National de la Recherche Scientifique (CNRS) and the Foundation for Fundamental Research on Matter supported by the Netherlands Organisation for Scientific Research, for the construction and operation of the Virgo detector and the creation and support of the EGO consortium. The authors also gratefully acknowledge research support from these agencies as well as by the Council of Scientific and Industrial Research of India, the Department of Science and Technology, India, the Science & Engineering Research Board (SERB), India, the Ministry of Human Resource Development, India, the Spanish Agencia Estatal de Investigación, the Vicepresidència i Conselleria d'Innovació, Recerca i Turisme and the Conselleria d'Educació i Universitat del Govern de les Illes Balears, the Conselleria d'Educació, Investigació, Cultura i Esport de la Generalitat Valenciana, the National Science Centre of Poland, the Swiss National Science Foundation (SNSF), the Russian Foundation for Basic Research, the Russian Science Foundation, the European Commission, the European Regional Development Funds (ERDF), the Royal Society, the Scottish Funding Council, the Scottish Universities Physics Alliance, the Hungarian Scientific Research Fund (OTKA), the Lyon Institute of Origins (LIO), the Paris Île-de-France Region, the National Research, Development and Innovation Office Hungary (NKFIH), the National Research Foundation of Korea, Industry Canada and the Province of Ontario through the Ministry of Economic Development and Innovation, the Natural Science and Engineering Research Council Canada, the Canadian Institute for Advanced Research, the Brazilian Ministry of Science, Technology, Innovations, and Communications, the International Center for Theoretical Physics South American Institute for Fundamental Research (ICTP-SAIFR), the Research Grants Council of Hong Kong, the National Natural Science Foundation of China (NSFC), the Leverhulme Trust, the Research Corporation, the Ministry of Science and Technology (MOST), Taiwan and the Kavli Foundation. The authors gratefully acknowledge the support of the NSF, STFC, MPS, INFN, CNRS, INFN-CNAF, PL-Grid, and the State of Niedersachsen/Germany for provision of computational resources. Work at SURFsara and Nikhef has been performed using resources of the Dutch e-Infrastructure, which is financially supported by the Nederlandse Organisatie voor Wetenschappelijk Onderzoek (Netherlands Organisation for Scientific Research, NWO) and the Dutch higher education and research partnership for network services and information and communication technology (SURF). This article has LIGO document number LIGO-P1900012-v7.

APPENDIX A

1. FrequencyHough hardware injections recovery

Table IX shows the parameters of the recovered signals, together with the error with respect to the injected signals. As shown in the Table, we have been able to detect all 13 injections done in the analyzed frequency band and the estimated parameters do show a very good agreement with the injected ones.

TABLE IX. Hardware injection recovery with the *FrequencyHough* pipeline. The reported values have been obtained at the end of the full analysis, including the follow-up. The values in parentheses are the absolute errors, that is the difference with respect to the injection parameters. The reference time is MJD 57856.826840. The sky position is given in equatorial coordinates.

Label	CR	Frequency [Hz]	Spin-down [nHz/s]	α [deg]	δ [deg]
ip13	27.8	12.427537(−0.000008)	−0.0070(0.0030)	11.14(−0.23)	17.78 (2.29)
ip10	147.8	26.338028(−0.000012)	−0.08423(0.00077)	221.14 (0.043)	42.79(−0.15)
ip11	130.8	31.424762 (0.000027)	−0.0009(0.0014)	284.52 (0.28)	−58.27(0.04)
ip12	78.7	38.192818(−0.000003)	−6.2542(−0.0042)	336.06 (2.24)	−25.74(−4.35)
ip5	161.9	52.808286(−0.000038)	0.00000 (4×10^{-9})	301.87(−0.37)	−83.641 (0.099)
ip3	67.42	108.857166(−0.000007)	−0.00088(−0.00088)	178.29(−0.0.2)	−33.59(−0.09)
ip6	76.4	145.862390 (0.000036)	−6.7245 (0.0055)	358.85 (0.27)	−65.63(−0.01)
ip8	72.7	190.636613(−0.000055)	−8.661(−0.011)	351.20(−0.08)	−33.04 (0.19)
ip0	293.6	265.575312(−0.000032)	0.0000 (0.0041)	71.64 (0.05)	−56.29(−0.03)
ip2	297.3	575.163534 (0.000019)	0.00000 (0.00014)	215.18 (0.03)	3.44(−0.02)
ip9	394.2	763.847307(−0.000010)	0.0053 (0.0053)	198.86(−0.01)	75.65(−0.02)
ip1	408.4	848.955908(−0.000048)	−0.2974 (0.0026)	37.43 (0.02)	−29.49(−0.02)

TABLE X. List of subthreshold candidates in the *FrequencyHough* analysis. Reference time is MJD 57856.826840. All parameters are averages of the values in each detector.

Order number	CR	Frequency [Hz]	Spin-down [nHz/s]	α [deg]	δ [deg]
1	4.75	184.0774	−5.0337	281.0392	−14.3215
2	4.63	294.6539	1.9496	314.7224	−1.3227
3	5.02	316.2952	−5.0802	237.2929	22.1560
4	4.46	339.3438	−2.9499	181.4295	33.5115
5	4.09	353.2267	−5.8594	346.0884	−27.8214
6	4.17	377.1483	−9.9569	261.5479	−33.9948
7	3.88	403.3479	1.8908	284.5725	−2.8764
8	4.29	404.0677	−3.3008	132.9264	−8.0342
9	4.11	423.3808	−0.0456	140.3369	83.1005
10	4.04	433.9027	0.2334	207.0290	−63.3601
11	4.26	457.7948	−2.1637	250.2473	12.2122
12	4.18	297.8762	−5.9050	116.5559	−37.5740
13	3.75	407.0068	0.8607	308.1622	41.2725
14	4.56	456.3493	−2.7138	270.8929	45.9713
15	3.59	475.5485	−7.0957	79.9163	−30.3946
16	4.60	475.7466	−1.0713	43.7284	−57.1093
17	3.18	611.3748	1.7294	111.7053	−31.0260
18	3.97	636.4725	−0.7449	161.4437	26.4633
19	3.33	636.4718	−0.8265	161.1148	27.2096
20	3.50	709.5682	−0.7265	75.0639	−57.6713
21	4.21	728.2990	0.7449	339.5191	−34.2676
22	3.92	739.6568	−0.0921	313.2296	−60.2544
23	3.69	821.2659	−1.2319	221.0008	27.1607
24	3.62	825.1451	−1.1582	74.7772	−34.8971
25	3.96	916.2110	1.6899	239.5039	27.3825
26	3.47	949.4410	−1.6215	155.2317	−28.9975

2. FrequencyHough selected subthreshold candidates

Table X shows the parameters of the candidates which have been excluded because, after the follow-up and the verification stages, are in coincidence (within the standard distance, equal to 3) but below the CR threshold value $CR_{thr} = 7.42$.

3. $\mathcal{F}$-statistic outliers

Table XI presents the parameters of the final 23 outliers from the *Time-domain $\mathcal{F}$-statistic* pipeline, along with comments on their likely causes. None is a credible gravitational wave signal.

TABLE XI. *Time-domain $\mathcal{F}$-statistic* pipeline outliers in the frequencies ranges [20–100], [100–434], and [1518–1922] Hz. The columns provide outliers false alarm probability (FAP) as well as the nominal frequencies and frequency derivatives, right ascensions and declinations found for the outliers, along with comments indicating the likely sources of the outliers. Frequencies are converted to epoch GPS 1174899130.

Index	FAP	Frequency [Hz]	Spin-down [nHz/s]	α [deg]	δ [deg]	Description
1	2.4×10^{-4}	21.428	0.014	−63.801	100.39	Present only in H1
2	1.1×10^{-4}	27.481	0.027	−63.159	272.42	Present only in L1
3	1.5×10^{-5}	29.970	−0.003	−66.303	89.028	Present only in H1
4	1.3×10^{-5}	31.764	0.030	−54.723	111.99	Interference much stronger in H1 than in L1
5	6.3×10^{-5}	39.763	0.015	−63.094	103.49	Interference much stronger in H1 than in L1
6	3.2×10^{-4}	42.945	0.015	−65.709	94.921	Present only in H1
7	4.5×10^{-5}	59.951	−0.026	−64.569	86.213	Present only in H1
8	$< 10^{-8}$	82.753	−4.229	−52.811	294.54	Interference stronger in H1 than in L1
9	1.3×10^{-4}	83.447	0.011	−65.403	94.618	Interference much stronger in H1 than in L1
10	2.6×10^{-4}	85.714	−0.003	−65.907	90.414	Present only in H1
11	1.6×10^{-4}	85.830	−0.004	−63.420	88.385	Present only in H1
12	$< 10^{-8}$	107.11	0.195	−6.0084	209.42	Present only in H1
13	$< 10^{-8}$	107.14	0.032	−6.4358	9.2631	Present only in H1
14	3.8×10^{-5}	119.90	0.046	−6.8506	9.3225	Interference stronger in H1 than in L1
15	$< 10^{-8}$	128.57	0.362	−7.0981	155.81	Present only in H1
16	$< 10^{-8}$	130.93	0.122	−5.2438	9.0533	Present only in H1
17	7.9×10^{-8}	199.86	−0.041	−8.1570	138.45	Present only in L1
18	1.6×10^{-8}	299.41	0.132	−8.2426	135.07	Present only in H1
19	$< 10^{-8}$	299.54	0.331	−7.0534	109.15	Present only in H1
20	$< 10^{-8}$	299.71	−0.229	−6.1941	7.7833	Present only in H1
21	1.3×10^{-7}	303.27	0.034	−3.4995	235.37	Present only in H1
22	$< 10^{-8}$	314.91	−0.145	−6.7862	7.9226	Present only in L1
23	$< 10^{-8}$	1800.1	−1.700	−68.404	75.855	Present only in L1

TABLE XII. Hardware injection recovery with the *Time-domain $\mathcal{F}$-statistic* pipeline. The values in parentheses are the absolute errors, that is, the difference with respect to the injection parameters. Frequencies are converted to epoch GPS 1174899130.

Label	FA	Frequency [Hz]	Spin-down [nHz/s]	α [deg]	δ [deg]
ip0	$< 10^{-8}$	265.5746 (0.0007)	−0.0466(−0.0425)	69.42 (2.12)	−57.21 (0.99)
ip3	$< 10^{-8}$	108.8573(−0.0001)	−0.1386 (0.1386)	174.96 (3.42)	−34.81(−1.37)
ip5	2.9×10^{-4}	52.8085 (0.0002)	−0.1865 (0.1865)	236.90 (65.72)	−74.18 (9.66)
ip6	$< 10^{-8}$	145.8721 (0.0048)	−6.0512 (0.6788)	358.75 (58.00)	−68.01 (2.58)
ip8	$< 10^{-8}$	190.6428 (0.0002)	−8.5306 (0.1193)	331.41 (19.98)	−35.87 (2.45)
ip10	2.2×10^{-4}	26.3380 (0.0001)	−0.0683 (0.0167)	223.10 (1.54)	37.23 (5.64)
ip11	4.0×10^{-4}	31.42475 (0.00001)	−0.0056 (0.0051)	286.25 (1.10)	−58.39 (0.11)
ip12	5.7×10^{-2}	38.2005 (0.0001)	−6.1165 (0.1335)	326.26 (5.60)	−33.71 (16.73)

[1] LIGO Scientific and Virgo Collaborations, GWTC-1: A gravitational-wave transient catalog of compact binary mergers observed by LIGO and Virgo during the first and second observing runs, arXiv:1811.12907.

[2] K. Riles, Recent searches for continuous gravitational waves, Mod. Phys. Lett. A **32**, 1730035 (2017).

[3] G. Woan, M. D. Pitkin, B. Haskell, D. I. Jones, and P. D. Lasky, Evidence for a minimum ellipticity in millisecond pulsars, Astrophys. J. Lett. **863**, L40 (2018).

[4] P. Lasky, Gravitational waves from neutron stars: A review, Pub. Astron. Soc. Aust. **32**, e034 (2015).

[5] B. P. Abbott *et al.* (LIGO Scientific Collaboration), Setting upper limits on the strength of periodic gravitational waves from PSR J1939+213, Phys. Rev. D **69**, 082004 (2004).

[6] B. P. Abbott *et al.* (LIGO Scientific Collaboration), Limits on Gravitational-Wave Emission from Selected Pulsars Using LIGO Data, Phys. Rev. Lett. **94**, 181103 (2005).

[7] B. P. Abbott *et al.* (LIGO Scientific Collaboration), Upper limits on gravitational wave emission from 78 radio pulsars, Phys. Rev. D **76**, 042001 (2007).

[8] B. P. Abbott *et al.* (LIGO Scientific Collaboration), Beating the spin-down limit on gravitational wave emission from the Crab pulsar, Astrophys. J. Lett. **683**, L45 (2008).

[9] B. P. Abbott *et al.* (LIGO Scientific and Virgo Collaborations), Searches for gravitational waves from known pulsars with S5 LIGO data, Astrophys. J. **713**, 671 (2010).

[10] J. Abadie *et al.* (LIGO Scientific and Virgo Collaborations), Beating the spin-down limit on gravitational wave emission from the Vela pulsar, Astrophys. J. **737**, 93 (2011).

[11] J. Aasi *et al.* (LIGO Scientific and Virgo Collaborations), Gravitational waves from known pulsars: Results from the initial detector era, Astrophys. J. **785**, 119 (2014).

[12] J. Aasi *et al.* (LIGO Scientific and Virgo Collaborations), Narrow-band search of continuous gravitational-wave signals from Crab and Vela pulsars in Virgo VSR4 data, Phys. Rev. D **91**, 022004 (2015).

[13] B. P. Abbott *et al.* (LIGO Scientific and Virgo Collaborations), First narrow-band search for continuous gravitational waves from known pulsars in advanced detector data, Phys. Rev. D **96**, 122006 (2017).

[14] B. P. Abbott *et al.* (LIGO Scientific and Virgo Collaborations), First search for gravitational waves from known pulsars with advanced LIGO, Astrophys. J. **839**, 12 (2017).

[15] B. P. Abbott *et al.* (LIGO Scientific and Virgo Collaborations), First Search for Nontensorial Gravitational Waves from Known Pulsars, Phys. Rev. Lett. **120**, 031104 (2018).

[16] B. P. Abbott *et al.* (LIGO Scientific Collaboration), Searches for periodic gravitational waves from unknown isolated sources and Scorpius X-1: Results from the second LIGO science run, Phys. Rev. D **76**, 082001 (2007).

[17] J. Abadie *et al.* (LIGO Scientific Collaboration), First search for gravitational waves from the youngest known neutron star, Astrophys. J. **722**, 1504 (2010).

[18] J. Aasi *et al.* (LIGO Scientific and Virgo Collaborations), Directed search for continuous gravitational waves from the Galactic center, Phys. Rev. D **88**, 102002 (2013).

[19] J. Aasi *et al.* (LIGO Scientific and Virgo Collaborations), Directed search for gravitational waves from Scorpius X-1 with initial LIGO data, Phys. Rev. D **91**, 062008 (2015).

[20] J. Aasi *et al.* (LIGO Scientific and Virgo Collaborations), Searches for continuous gravitational waves from nine young supernova remnants, Astrophys. J. **813**, 39 (2015).

[21] J. Aasi *et al.* (LIGO Scientific and Virgo Collaborations), A search of the Orion spur for continuous gravitational waves using a loosely coherent algorithm on data from LIGO interferometers, Phys. Rev. D **93**, 042006 (2016).

[22] L. Sun, A. Melatos, P. D. Lasky, C. T. Y. Chung, and N. S. Darman, Cross-correlation search for continuous gravitational waves from a compact object in SNR 1987A in LIGO Science run 5, Phys. Rev. D **94**, 082004 (2016).

[23] G. D. Meadors, E. Goetz, K. Riles, T. Creighton, and F. Robinet, Searches for continuous gravitational waves from Scorpius X-1 and XTE J1751-305 in LIGO's sixth science run, Phys. Rev. D **95**, 042005 (2017).

[24] B. P. Abbott *et al.* (LIGO Scientific and Virgo Collaborations), Search for continuous gravitational waves from neutron stars in globular cluster NGC 6544, Phys. Rev. D **95**, 082005 (2017).

[25] B. P. Abbott *et al.* (LIGO Scientific and Virgo Collaborations), Search for gravitational waves from Scorpius X-1 in the first Advanced LIGO observing run with a hidden Markov model, Phys. Rev. D **95**, 122003 (2017).

[26] B. P. Abbott *et al.* (LIGO Scientific and Virgo Collaborations), Upper limits on gravitational waves from Scorpius X-1 from a model-based cross-correlation search in advanced LIGO data, Astrophys. J. **847**, 47 (2017).

[27] B. P. Abbott *et al.* (LIGO Scientific Collaboration), First all-sky upper limits from LIGO on the strength of periodic gravitational waves using the Hough transform, Phys. Rev. D **72**, 102004 (2005).

[28] B. P. Abbott *et al.* (LIGO Scientific Collaboration), All-sky search for periodic gravitational waves in LIGO S4 data, Phys. Rev. D **77**, 022001 (2008).

[29] B. P. Abbott *et al.* (LIGO Scientific Collaboration), Einstein@Home search for periodic gravitational waves in LIGO S4 data, Phys. Rev. D **79**, 022001 (2009).

[30] B. P. Abbott *et al.* (LIGO and Virgo Scientific Collaborations), All-sky search for periodic gravitational waves in the full S5 data, Phys. Rev. D **85**, 022001 (2012).

[31] B. P. Abbott *et al.* (LIGO Scientific Collaboration), Einstein@Home all-sky search for periodic gravitational waves in LIGO S5 data, Phys. Rev. D **87**, 042001 (2013).

[32] J. Aasi (LIGO Scientific and Virgo Collaborations), Application of a Hough search for continuous gravitational waves on data from the 5th LIGO science run, Classical Quantum Gravity **31**, 085014 (2014).

[33] J. Aasi *et al.* (LIGO Scientific and Virgo Collaborations), Implementation of an $\mathcal{F}$-statistic all-sky search for continuous gravitational waves in Virgo VSR1 data, Classical Quantum Gravity **31**, 165014 (2014).

[34] J. Aasi *et al.* (LIGO Scientific and Virgo Collaborations), First all-sky search for continuous gravitational waves from

unknown sources in binary systems, Phys. Rev. D **90**, 062010 (2014).
[35] J. Aasi *et al.* (LIGO Scientific and Virgo Collaborations), Comprehensive all-sky search for periodic gravitational waves in the sixth science run LIGO data, Phys. Rev. D **94**, 042002 (2016).
[36] J. Aasi *et al.* (LIGO Scientific and Virgo Collaborations), First low-frequency all-sky search for continuous gravitational wave signals, Phys. Rev. D **93**, 042007 (2016).
[37] B. P. Abbott *et al.* (LIGO Scientific and Virgo Collaborations), Results of the deepest all-sky survey for continuous gravitational waves on LIGO S6 data, Phys. Rev. D **94**, 102002 (2016).
[38] B. P. Abbott *et al.* (LIGO Scientific and Virgo Collaborations), All-sky search for periodic gravitational waves in the O1 LIGO data, Phys. Rev. D **96**, 062002 (2017).
[39] B. P. Abbott *et al.* (LIGO Scientific and Virgo Collaborations), First low-frequency Einstein@Home all-sky search for continuous gravitational waves in Advanced LIGO data, Phys. Rev. D **96**, 122004 (2017).
[40] B. P. Abbott *et al.* (LIGO Scientific and Virgo Collaborations), Full band all-sky search for periodic gravitational waves in the O1 LIGO data, Phys. Rev. D **97**, 102003 (2018).
[41] P. Astone, A. Colla, S. D'Antonio, S. Frasca, and C. Palomba, Method for all-sky searches of continuous gravitational wave signals using the FrequencyHough transform, Phys. Rev. D **90**, 042002 (2014).
[42] B. Krishnan, A. M. Sintes, M. Alessandra Papa, B. F. Schutz, S. Frasca, and C. Palomba, Hough transform search for continuous gravitational waves, Phys. Rev. D **70**, 082001 (2004).
[43] P. Jaranowski, A. Królak, and B. F. Schutz, Data analysis of gravitational-wave signals from spinning neutron stars: The signal and its detection, Phys. Rev. D **58**, 063001 (1998).
[44] J. Aasi *et al.* (LIGO Scientific Collaboration), Advanced LIGO, Classical Quantum Gravity **32**, 115012 (2015).
[45] F. Acernese *et al.* (Virgo Collaboration), Advanced Virgo: A second-generation interferometric gravitational wave detector, Classical Quantum Gravity **32**, 024001 (2015).
[46] P. B. Covas *et al.* (LSC Instrument Authors), Identification and mitigation of narrow spectral artifacts that degrade searches for persistent gravitational waves in the first two observing runs of Advanced LIGO, Phys. Rev. D **97**, 082002 (2018).
[47] J. C. Driggers *et al.* (LIGO Scientific Collaboration Instrument Science Authors), Improving astrophysical parameter estimation via offline noise substraction for Advancd LIGO, Phys. Rev. D **99**, 042001 (2019).
[48] C. Cahillane, J. Betzwieser, D. A. Brown, E. Goetz, E. D. Hall, K. Izumi, S. Kandhasamy, S. Karki, J. S. Kissel, G. Mendell, R. L. Savage, D. Tuyenbayev, A. Urban, A. Viets, M. Wade, and A. J. Weinstein, Calibration uncertainty for Advanced LIGO's first and second observing runs, Phys. Rev. D **96**, 102001 (2017).
[49] P. Leaci, P. Astone, S. D'Antonio, S. Frasca, C. Palomba, O. J. Piccinni, and S. Mastrogiovanni, Novel directed search strategy to detect continuous gravitational waves from neutron stars in low- and high-eccentricity binary systems, Phys. Rev. D **95**, 122001 (2017).
[50] F. Antonucci, P. Astone, S. D'Antonio, S. Frasca, and C. Palomba, Detection of periodic gravitational wave sources by Hough transform in the f versus $\dot{f}$ plane, Classical Quantum Gravity **25**, 184015 (2008).
[51] P. Astone, S. Frasca, and C. Palomba, The short FFT database and the peak map for the hierarchical search of periodic sources, Classical Quantum Gravity **22**, S1197 (2005).
[52] C. Palomba, P. Astone, and S. Frasca, Adaptive Hough transform for the search of periodic sources, Classical Quantum Gravity **22**, S1255 (2005).
[53] O. J. Piccinni, P. Astone, S. D'Antonio, S. Frasca, G. Intini, P. Leaci, S. Mastrogiovanni, A. Miller, C. Palomba, and A. Singhal, A new data analysis framework for the search of continuous gravitational wave signals, Classical Quantum Gravity **36**, 015008 (2019).
[54] P. Astone, S. D' Antonio, S. Frasca, and C. Palomba, A method for detection of known sources of continuous gravitational wave signals in nonstationary data, Classical Quantum Gravity **27**, 194016 (2010).
[55] LIGO Scientific Collaboration, LIGO Algorithm Library, https://doi.org/10.7935/GT1W-FZ16 (2018).
[56] A. M. Sintes and B. Krishnan, Hough search with improved sensitivity, Technical Report No. LIGO-T070124, 2007.
[57] H. J. Pletsch, Parameter-space metric of semicoherent searches for continuous gravitational waves, Phys. Rev. D **82**, 042002 (2010).
[58] M. Alessandra Papa *et al.*, Hierarchical follow-up of subthreshold candidates of an all-sky Einstein@Home search for continuous gravitational waves on LIGO sixth science run data, Phys. Rev. D **94**, 122006 (2016).
[59] G. Ashton and R. Prix, Hierarchical multistage MCMC follow-up of continuous gravitational wave candidates, Phys. Rev. D **97**, 103020 (2018).
[60] P. Astone, K. M. Borkowski, P. Jaranowski, M. Pietka, and A. Królak, Data analysis of gravitational-wave signals from spinning neutron stars. V. A narrow-band all-sky search, Phys. Rev. D **82**, 022005 (2010).
[61] A. Pisarski and P. Jaranowski, Banks of templates for all-sky narrow-band searches of gravitational waves from spinning neutron stars, Classical Quantum Gravity **32**, 145014 (2015).
[62] V. Dergachev and M. Alessandra Papa, First loosely coherent all-sky search for periodic gravitational waves in the O1 LIGO data, arXiv:1902.05530.
[63] B. P. Abbott *et al.* (LIGO Scientific and Virgo Collaborations), Searches for gravitational-waves from known pulsars in 2015-2017 LIGO data, arXiv:1902.08507.
[64] EGI, https://www.egi.eu.
[65] R. Prix, Gravitational waves from spinning neutron stars, Astrophys. Space Sci. Libr. **357**, 651 (2009).
[66] R. Prix and M. Shaltev, Search for continuous gravitational waves: Optimal StackSlide method at fixed computing cost, Phys. Rev. D **85**, 084010 (2012).

[67] K. Wette, Estimating the sensitivity of wide-parameter-space searches for gravitational-wave pulsars, Phys. Rev. D **85**, 042003 (2012).

[68] N. K. Johnson-McDaniel and B. J. Owen, Maximum elastic deformations of relativistic stars, Phys. Rev. D **88**, 044004 (2013).

B. P. Abbott,[1] R. Abbott,[1] T. D. Abbott,[2] S. Abraham,[3] F. Acernese,[4,5] K. Ackley,[6] C. Adams,[7] R. X. Adhikari,[1] V. B. Adya,[8,9] C. Affeldt,[8,9] M. Agathos,[10] K. Agatsuma,[11] N. Aggarwal,[12] O. D. Aguiar,[13] L. Aiello,[14,15] A. Ain,[3] P. Ajith,[16] G. Allen,[17] A. Allocca,[18,19] M. A. Aloy,[20] P. A. Altin,[21] A. Amato,[22] A. Ananyeva,[1] S. B. Anderson,[1] W. G. Anderson,[23] S. V. Angelova,[24] S. Antier,[25] S. Appert,[1] K. Arai,[1] M. C. Araya,[1] J. S. Areeda,[26] M. Arène,[27] N. Arnaud,[25,28] K. G. Arun,[29] S. Ascenzi,[30,31] G. Ashton,[6] S. M. Aston,[7] P. Astone,[32] F. Aubin,[33] P. Aufmuth,[9] K. AultONeal,[34] C. Austin,[2] V. Avendano,[35] A. Avila-Alvarez,[26] S. Babak,[36,27] P. Bacon,[27] F. Badaracco,[14,15] M. K. M. Bader,[37] S. Bae,[38] P. T. Baker,[39] F. Baldaccini,[40,41] G. Ballardin,[28] S. W. Ballmer,[42] S. Banagiri,[43] J. C. Barayoga,[1] S. E. Barclay,[44] B. C. Barish,[1] D. Barker,[45] K. Barkett,[46] S. Barnum,[12] F. Barone,[4,5] B. Barr,[44] L. Barsotti,[12] M. Barsuglia,[27] D. Barta,[47] J. Bartlett,[45] I. Bartos,[48] R. Bassiri,[49] A. Basti,[18,19] M. Bawaj,[50,41] J. C. Bayley,[44] M. Bazzan,[51,52] B. Bécsy,[53] M. Bejger,[27,54] I. Belahcene,[25] A. S. Bell,[44] D. Beniwal,[55] B. K. Berger,[49] G. Bergmann,[8,9] S. Bernuzzi,[56,57] J. J. Bero,[58] C. P. L. Berry,[59] D. Bersanetti,[60] A. Bertolini,[37] J. Betzwieser,[7] R. Bhandare,[61] J. Bidler,[26] I. A. Bilenko,[62] S. A. Bilgili,[39] G. Billingsley,[1] J. Birch,[7] R. Birney,[24] O. Birnholtz,[58] S. Biscans,[1,12] S. Biscoveanu,[6] A. Bisht,[9] M. Bitossi,[28,19] M. A. Bizouard,[25] J. K. Blackburn,[1] C. D. Blair,[7] D. G. Blair,[63] R. M. Blair,[45] S. Bloemen,[64] N. Bode,[8,9] M. Boer,[65] Y. Boetzel,[66] G. Bogaert,[65] F. Bondu,[67] E. Bonilla,[49] R. Bonnand,[33] P. Booker,[8,9] B. A. Boom,[37] C. D. Booth,[68] R. Bork,[1] V. Boschi,[28] S. Bose,[69,3] K. Bossie,[7] V. Bossilkov,[63] J. Bosveld,[63] Y. Bouffanais,[27] A. Bozzi,[28] C. Bradaschia,[19] P. R. Brady,[23] A. Bramley,[7] M. Branchesi,[14,15] J. E. Brau,[70] T. Briant,[71] J. H. Briggs,[44] F. Brighenti,[72,73] A. Brillet,[65] M. Brinkmann,[8,9] V. Brisson,[25,†] P. Brockill,[23] A. F. Brooks,[1] D. D. Brown,[55] S. Brunett,[1] A. Buikema,[12] T. Bulik,[74] H. J. Bulten,[75,37] A. Buonanno,[36,76] D. Buskulic,[33] C. Buy,[27] R. L. Byer,[49] M. Cabero,[8,9] L. Cadonati,[77] G. Cagnoli,[22,78] C. Cahillane,[1] J. Calderón Bustillo,[6] T. A. Callister,[1] E. Calloni,[79,5] J. B. Camp,[80] W. A. Campbell,[6] K. C. Cannon,[81] H. Cao,[55] J. Cao,[82] E. Capocasa,[27] F. Carbognani,[28] S. Caride,[83] M. F. Carney,[59] G. Carullo,[18] J. Casanueva Diaz,[19] C. Casentini,[30,31] S. Caudill,[37] M. Cavaglià,[84] F. Cavalier,[25] R. Cavalieri,[28] G. Cella,[19] P. Cerdá-Durán,[20] G. Cerretani,[18,19] E. Cesarini,[85,31] O. Chaibi,[65] K. Chakravarti,[3] S. J. Chamberlin,[86] M. Chan,[44] S. Chao,[87] P. Charlton,[88] E. A. Chase,[59] E. Chassande-Mottin,[27] D. Chatterjee,[23] M. Chaturvedi,[61] K. Chatziioannou,[89] B. D. Cheeseboro,[39] H. Y. Chen,[90] X. Chen,[63] Y. Chen,[46] H.-P. Cheng,[48] C. K. Cheong,[91] H. Y. Chia,[48] A. Chincarini,[60] A. Chiummo,[28] G. Cho,[92] H. S. Cho,[93] M. Cho,[76] N. Christensen,[65,94] Q. Chu,[63] S. Chua,[71] K. W. Chung,[91] S. Chung,[63] G. Ciani,[51,52] P. Ciecielag,[54] A. A. Ciobanu,[55] R. Ciolfi,[95,96] F. Cipriano,[65] A. Cirone,[97,60] F. Clara,[45] J. A. Clark,[77] P. Clearwater,[98] F. Cleva,[65] C. Cocchieri,[84] E. Coccia,[14,15] P.-F. Cohadon,[71] D. Cohen,[25] R. Colgan,[99] M. Colleoni,[100] C. G. Collette,[101] C. Collins,[11] L. R. Cominsky,[102] M. Constancio Jr.,[13] L. Conti,[52] S. J. Cooper,[11] P. Corban,[7] T. R. Corbitt,[2] I. Cordero-Carrión,[103] K. R. Corley,[99] N. Cornish,[53] A. Corsi,[83] S. Cortese,[28] C. A. Costa,[13] R. Cotesta,[36] M. W. Coughlin,[1] S. B. Coughlin,[68,59] J.-P. Coulon,[65] S. T. Countryman,[99] P. Couvares,[1] P. B. Covas,[100] E. E. Cowan,[77] D. M. Coward,[63] M. J. Cowart,[7] D. C. Coyne,[1] R. Coyne,[104] J. D. E. Creighton,[23] T. D. Creighton,[105] J. Cripe,[2] M. Croquette,[71] S. G. Crowder,[106] T. J. Cullen,[2] A. Cumming,[44] L. Cunningham,[44] E. Cuoco,[28] T. Dal Canton,[80] G. Dálya,[107] S. L. Danilishin,[8,9] S. D'Antonio,[31] K. Danzmann,[9,8] A. Dasgupta,[108] C. F. Da Silva Costa,[48] L. E. H. Datrier,[44] V. Dattilo,[28] I. Dave,[61] M. Davier,[25] D. Davis,[42] E. J. Daw,[109] D. DeBra,[49] M. Deenadayalan,[3] J. Degallaix,[22] M. De Laurentis,[79,5] S. Deléglise,[71] W. Del Pozzo,[18,19] L. M. DeMarchi,[59] N. Demos,[12] T. Dent,[8,9,110] R. De Pietri,[111,57] J. Derby,[26] R. De Rosa,[79,5] C. De Rossi,[22,28] R. DeSalvo,[112] O. de Varona,[8,9] S. Dhurandhar,[3] M. C. Díaz,[105] T. Dietrich,[37] L. Di Fiore,[5] M. Di Giovanni,[113,96] T. Di Girolamo,[79,5] A. Di Lieto,[18,19] B. Ding,[101] S. Di Pace,[114,32] I. Di Palma,[114,32] F. Di Renzo,[18,19] A. Dmitriev,[11] Z. Doctor,[90] F. Donovan,[12] K. L. Dooley,[68,84] S. Doravari,[8,9] O. Dorosh,[115] I. Dorrington,[68] T. P. Downes,[23] M. Drago,[14,15] J. C. Driggers,[45] Z. Du,[82] J.-G. Ducoin,[25] P. Dupej,[44] S. E. Dwyer,[45] P. J. Easter,[6] T. B. Edo,[109] M. C. Edwards,[94] A. Effler,[7] P. Ehrens,[1] J. Eichholz,[1] S. S. Eikenberry,[48] M. Eisenmann,[33] R. A. Eisenstein,[12] R. C. Essick,[90] H. Estelles,[100] D. Estevez,[33] Z. B. Etienne,[39] T. Etzel,[1] M. Evans,[12] T. M. Evans,[7] V. Fafone,[30,31,14] H. Fair,[42] S. Fairhurst,[68] X. Fan,[82] S. Farinon,[60] B. Farr,[70] W. M. Farr,[11] E. J. Fauchon-Jones,[68] M. Favata,[35] M. Fays,[109] M. Fazio,[116] C. Fee,[117] J. Feicht,[1] M. M. Fejer,[49] F. Feng,[27] A. Fernandez-Galiana,[12] I. Ferrante,[18,19] E. C. Ferreira,[13] T. A. Ferreira,[13] F. Ferrini,[28] F. Fidecaro,[18,19] I. Fiori,[28]

D. Fiorucci,[27] M. Fishbach,[90] R. P. Fisher,[42,118] J. M. Fishner,[12] M. Fitz-Axen,[43] R. Flaminio,[33,119] M. Fletcher,[44] E. Flynn,[26] H. Fong,[89] J. A. Font,[20,120] P. W. F. Forsyth,[21] J.-D. Fournier,[65] S. Frasca,[114,32] F. Frasconi,[19] Z. Frei,[107] A. Freise,[11] R. Frey,[70] V. Frey,[25] P. Fritschel,[12] V. V. Frolov,[7] P. Fulda,[48] M. Fyffe,[7] H. A. Gabbard,[44] B. U. Gadre,[3] S. M. Gaebel,[11] J. R. Gair,[121] L. Gammaitoni,[40] M. R. Ganija,[55] S. G. Gaonkar,[3] A. Garcia,[26] C. García-Quirós,[100] F. Garufi,[79,5] B. Gateley,[45] S. Gaudio,[34] G. Gaur,[122] V. Gayathri,[123] G. Gemme,[60] E. Genin,[28] A. Gennai,[19] D. George,[17] J. George,[61] L. Gergely,[124] V. Germain,[33] S. Ghonge,[77] Abhirup Ghosh,[16] Archisman Ghosh,[37] S. Ghosh,[23] B. Giacomazzo,[113,96] J. A. Giaime,[2,7] K. D. Giardina,[7] A. Giazotto,[19,†] K. Gill,[34] G. Giordano,[4,5] L. Glover,[112] P. Godwin,[86] E. Goetz,[45] R. Goetz,[48] B. Goncharov,[6] G. González,[2] J. M. Gonzalez Castro,[18,19] A. Gopakumar,[125] M. L. Gorodetsky,[62] S. E. Gossan,[1] M. Gosselin,[28] R. Gouaty,[33] A. Grado,[126,5] C. Graef,[44] M. Granata,[22] A. Grant,[44] S. Gras,[12] P. Grassia,[1] C. Gray,[45] R. Gray,[44] G. Greco,[72,73] A. C. Green,[11,48] R. Green,[68] E. M. Gretarsson,[34] P. Groot,[64] H. Grote,[68] S. Grunewald,[36] P. Gruning,[25] G. M. Guidi,[72,73] H. K. Gulati,[108] Y. Guo,[37] A. Gupta,[86] M. K. Gupta,[108] E. K. Gustafson,[1] R. Gustafson,[127] L. Haegel,[100] O. Halim,[15,14] B. R. Hall,[69] E. D. Hall,[12] E. Z. Hamilton,[68] G. Hammond,[44] M. Haney,[66] M. M. Hanke,[8,9] J. Hanks,[45] C. Hanna,[86] M. D. Hannam,[68] O. A. Hannuksela,[91] J. Hanson,[7] T. Hardwick,[2] K. Haris,[16] J. Harms,[14,15] G. M. Harry,[128] I. W. Harry,[36] B. Haskell,[54] C.-J. Haster,[89] K. Haughian,[44] F. J. Hayes,[44] J. Healy,[58] A. Heidmann,[71] M. C. Heintze,[7] H. Heitmann,[65] P. Hello,[25] G. Hemming,[28] M. Hendry,[44] I. S. Heng,[44] J. Hennig,[8,9] A. W. Heptonstall,[1] Francisco Hernandez Vivanco,[6] M. Heurs,[8,9] S. Hild,[44] T. Hinderer,[129,37,130] D. Hoak,[28] S. Hochheim,[8,9] D. Hofman,[22] A. M. Holgado,[17] N. A. Holland,[21] K. Holt,[7] D. E. Holz,[90] P. Hopkins,[68] C. Horst,[23] J. Hough,[44] S. Hourihane,[127] E. J. Howell,[63] C. G. Hoy,[68] A. Hreibi,[65] E. A. Huerta,[17] D. Huet,[25] B. Hughey,[34] M. Hulko,[1] S. Husa,[100] S. H. Huttner,[44] T. Huynh-Dinh,[7] B. Idzkowski,[74] A. Iess,[30,31] C. Ingram,[55] R. Inta,[83] G. Intini,[114,32] B. Irwin,[117] H. N. Isa,[44] J.-M. Isac,[71] M. Isi,[1] B. R. Iyer,[16] K. Izumi,[45] T. Jacqmin,[71] S. J. Jadhav,[131] K. Jani,[77] N. N. Janthalur,[131] P. Jaranowski,[132] A. C. Jenkins,[133] J. Jiang,[48] D. S. Johnson,[17] A. W. Jones,[11] D. I. Jones,[134] R. Jones,[44] R. J. G. Jonker,[37] L. Ju,[63] J. Junker,[8,9] C. V. Kalaghatgi,[68] V. Kalogera,[59] B. Kamai,[1] S. Kandhasamy,[84] G. Kang,[38] J. B. Kanner,[1] S. J. Kapadia,[23] S. Karki,[70] K. S. Karvinen,[8,9] R. Kashyap,[16] M. Kasprzack,[1] S. Katsanevas,[28] E. Katsavounidis,[12] W. Katzman,[7] S. Kaufer,[9] K. Kawabe,[45] N. V. Keerthana,[3] F. Kéfélian,[65] D. Keitel,[44] R. Kennedy,[109] J. S. Key,[135] F. Y. Khalili,[62] H. Khan,[26] I. Khan,[14,31] S. Khan,[8,9] Z. Khan,[108] E. A. Khazanov,[136] M. Khursheed,[61] N. Kijbunchoo,[21] Chunglee Kim,[137] J. C. Kim,[138] K. Kim,[91] W. Kim,[55] W. S. Kim,[139] Y.-M. Kim,[140] C. Kimball,[59] E. J. King,[55] P. J. King,[45] M. Kinley-Hanlon,[128] R. Kirchhoff,[8,9] J. S. Kissel,[45] L. Kleybolte,[141] J. H. Klika,[23] S. Klimenko,[48] T. D. Knowles,[39] P. Koch,[8,9] S. M. Koehlenbeck,[8,9] G. Koekoek,[37,142] S. Koley,[37] V. Kondrashov,[1] A. Kontos,[12] N. Koper,[8,9] M. Korobko,[141] W. Z. Korth,[1] I. Kowalska,[74] D. B. Kozak,[1] V. Kringel,[8,9] N. Krishnendu,[29] A. Królak,[115,143] G. Kuehn,[8,9] A. Kumar,[131] P. Kumar,[144] R. Kumar,[108] S. Kumar,[16] L. Kuo,[87] A. Kutynia,[115] S. Kwang,[23] B. D. Lackey,[36] K. H. Lai,[91] T. L. Lam,[91] M. Landry,[45] B. B. Lane,[12] R. N. Lang,[145] J. Lange,[58] B. Lantz,[49] R. K. Lanza,[12] A. Lartaux-Vollard,[25] P. D. Lasky,[6] M. Laxen,[7] A. Lazzarini,[1] C. Lazzaro,[52] P. Leaci,[114,32] S. Leavey,[8,9] Y. K. Lecoeuche,[45] C. H. Lee,[93] H. K. Lee,[146] H. M. Lee,[147] H. W. Lee,[138] J. Lee,[92] K. Lee,[44] J. Lehmann,[8,9] A. Lenon,[39] N. Leroy,[25] N. Letendre,[33] Y. Levin,[6,99] J. Leviton,[127] J. Li,[82] K. J. L. Li,[91] T. G. F. Li,[91] X. Li,[46] F. Lin,[6] F. Linde,[37] S. D. Linker,[112] T. B. Littenberg,[148] J. Liu,[63] X. Liu,[23] R. K. L. Lo,[91,1] N. A. Lockerbie,[24] L. T. London,[68] A. Longo,[149,150] M. Lorenzini,[14,15] V. Loriette,[151] M. Lormand,[7] G. Losurdo,[19] J. D. Lough,[8,9] C. O. Lousto,[58] G. Lovelace,[26] M. E. Lower,[152] H. Lück,[9,8] D. Lumaca,[30,31] A. P. Lundgren,[153] R. Lynch,[12] Y. Ma,[46] R. Macas,[68] S. Macfoy,[24] M. MacInnis,[12] D. M. Macleod,[68] A. Macquet,[65] F. Magaña-Sandoval,[42] L. Magaña Zertuche,[84] R. M. Magee,[86] E. Majorana,[32] I. Maksimovic,[151] A. Malik,[61] N. Man,[65] V. Mandic,[43] V. Mangano,[44] G. L. Mansell,[45,12] M. Manske,[23,21] M. Mantovani,[28] F. Marchesoni,[50,41] F. Marion,[33] S. Márka,[99] Z. Márka,[99] C. Markakis,[10,17] A. S. Markosyan,[49] A. Markowitz,[1] E. Maros,[1] A. Marquina,[103] S. Marsat,[36] F. Martelli,[72,73] I. W. Martin,[44] R. M. Martin,[35] D. V. Martynov,[11] K. Mason,[12] E. Massera,[109] A. Masserot,[33] T. J. Massinger,[1] M. Masso-Reid,[44] S. Mastrogiovanni,[114,32] A. Matas,[43,36] F. Matichard,[1,12] L. Matone,[99] N. Mavalvala,[12] N. Mazumder,[69] J. J. McCann,[63] R. McCarthy,[45] D. E. McClelland,[21] S. McCormick,[7] L. McCuller,[12] S. C. McGuire,[154] J. McIver,[1] D. J. McManus,[21] T. McRae,[21] S. T. McWilliams,[39] D. Meacher,[86] G. D. Meadors,[6] M. Mehmet,[8,9] A. K. Mehta,[16] J. Meidam,[37] A. Melatos,[98] G. Mendell,[45] R. A. Mercer,[23] L. Mereni,[22] E. L. Merilh,[45] M. Merzougui,[65] S. Meshkov,[1] C. Messenger,[44] C. Messick,[86] R. Metzdorff,[71] P. M. Meyers,[98] H. Miao,[11] C. Michel,[22] H. Middleton,[98] E. E. Mikhailov,[155] L. Milano,[79,5] A. L. Miller,[48] A. Miller,[114,32] M. Millhouse,[53] J. C. Mills,[68] M. C. Milovich-Goff,[112] O. Minazzoli,[65,156] Y. Minenkov,[31] A. Mishkin,[48] C. Mishra,[157] T. Mistry,[109] S. Mitra,[3] V. P. Mitrofanov,[62] G. Mitselmakher,[48] R. Mittleman,[12] G. Mo,[94] D. Moffa,[117] K. Mogushi,[84] S. R. P. Mohapatra,[12] M. Montani,[72,73] C. J. Moore,[10] D. Moraru,[45] G. Moreno,[45] S. Morisaki,[81] B. Mours,[33] C. M. Mow-Lowry,[11] Arunava Mukherjee,[8,9]

D. Mukherjee,[23] S. Mukherjee,[105] N. Mukund,[3] A. Mullavey,[7] J. Munch,[55] E. A. Muñiz,[42] M. Muratore,[34] P. G. Murray,[44] I. Nardecchia,[30,31] L. Naticchioni,[114,32] R. K. Nayak,[158] J. Neilson,[112] G. Nelemans,[64,37] T. J. N. Nelson,[7] M. Nery,[8,9] A. Neunzert,[127] K. Y. Ng,[12] S. Ng,[55] P. Nguyen,[70] D. Nichols,[129,37] S. Nissanke,[129,37] F. Nocera,[28] C. North,[68] L. K. Nuttall,[153] M. Obergaulinger,[20] J. Oberling,[45] B. D. O'Brien,[48] G. D. O'Dea,[112] G. H. Ogin,[159] J. J. Oh,[139] S. H. Oh,[139] F. Ohme,[8,9] H. Ohta,[81] M. A. Okada,[13] M. Oliver,[100] P. Oppermann,[8,9] Richard J. Oram,[7] B. O'Reilly,[7] R. G. Ormiston,[43] L. F. Ortega,[48] R. O'Shaughnessy,[58] S. Ossokine,[36] D. J. Ottaway,[55] H. Overmier,[7] B. J. Owen,[83] A. E. Pace,[86] G. Pagano,[18,19] M. A. Page,[63] A. Pai,[123] S. A. Pai,[61] J. R. Palamos,[70] O. Palashov,[136] C. Palomba,[32] A. Pal-Singh,[141] Huang-Wei Pan,[87] B. Pang,[46] P. T. H. Pang,[91] C. Pankow,[59] F. Pannarale,[114,32] B. C. Pant,[61] F. Paoletti,[19] A. Paoli,[28] A. Parida,[3] W. Parker,[7,154] D. Pascucci,[44] A. Pasqualetti,[28] R. Passaquieti,[18,19] D. Passuello,[19] M. Patil,[143] B. Patricelli,[18,19] B. L. Pearlstone,[44] C. Pedersen,[68] M. Pedraza,[1] R. Pedurand,[22,160] A. Pele,[7] S. Penn,[161] C. J. Perez,[45] A. Perreca,[113,96] H. P. Pfeiffer,[36,89] M. Phelps,[8,9] K. S. Phukon,[3] O. J. Piccinni,[114,32] M. Pichot,[65] F. Piergiovanni,[72,73] G. Pillant,[28] L. Pinard,[22] M. Pirello,[45] M. Pitkin,[44] R. Poggiani,[18,19] D. Y. T. Pong,[91] S. Ponrathnam,[3] P. Popolizio,[28] E. K. Porter,[27] J. Powell,[152] A. K. Prajapati,[108] J. Prasad,[3] K. Prasai,[49] R. Prasanna,[131] G. Pratten,[100] T. Prestegard,[23] S. Privitera,[36] G. A. Prodi,[113,96] L. G. Prokhorov,[62] O. Puncken,[8,9] M. Punturo,[41] P. Puppo,[32] M. Pürrer,[36] H. Qi,[23] V. Quetschke,[105] P. J. Quinonez,[34] E. A. Quintero,[1] R. Quitzow-James,[70] F. J. Raab,[45] H. Radkins,[45] N. Radulescu,[65] P. Raffai,[107] S. Raja,[61] C. Rajan,[61] B. Rajbhandari,[83] M. Rakhmanov,[105] K. E. Ramirez,[105] A. Ramos-Buades,[100] Javed Rana,[3] K. Rao,[59] P. Rapagnani,[114,32] V. Raymond,[68] M. Razzano,[18,19] J. Read,[26] T. Regimbau,[33] L. Rei,[60] S. Reid,[24] D. H. Reitze,[1,48] W. Ren,[17] F. Ricci,[114,32] C. J. Richardson,[34] J. W. Richardson,[1] P. M. Ricker,[17] K. Riles,[127] M. Rizzo,[59] N. A. Robertson,[1,44] R. Robie,[44] F. Robinet,[25] A. Rocchi,[31] L. Rolland,[33] J. G. Rollins,[1] V. J. Roma,[70] M. Romanelli,[67] R. Romano,[4,5] C. L. Romel,[45] J. H. Romie,[7] K. Rose,[117] D. Rosińska,[162,54] S. G. Rosofsky,[17] M. P. Ross,[163] S. Rowan,[44] A. Rüdiger,[8,9,†] P. Ruggi,[28] G. Rutins,[164] K. Ryan,[45] S. Sachdev,[1] T. Sadecki,[45] M. Sakellariadou,[133] L. Salconi,[28] M. Saleem,[29] A. Samajdar,[37] L. Sammut,[6] E. J. Sanchez,[1] L. E. Sanchez,[1] N. Sanchis-Gual,[20] V. Sandberg,[45] J. R. Sanders,[42] K. A. Santiago,[35] N. Sarin,[6] B. Sassolas,[22] B. S. Sathyaprakash,[86,68] P. R. Saulson,[42] O. Sauter,[127] R. L. Savage,[45] P. Schale,[70] M. Scheel,[46] J. Scheuer,[59] P. Schmidt,[64] R. Schnabel,[141] R. M. S. Schofield,[70] A. Schönbeck,[141] E. Schreiber,[8,9] B. W. Schulte,[8,9] B. F. Schutz,[68] S. G. Schwalbe,[34] J. Scott,[44] S. M. Scott,[21] E. Seidel,[17] D. Sellers,[7] A. S. Sengupta,[165] N. Sennett,[36] D. Sentenac,[28] V. Sequino,[30,31,14] A. Sergeev,[136] Y. Setyawati,[8,9] D. A. Shaddock,[21] T. Shaffer,[45] M. S. Shahriar,[59] M. B. Shaner,[112] L. Shao,[36] P. Sharma,[61] P. Shawhan,[76] H. Shen,[17] R. Shink,[166] D. H. Shoemaker,[12] D. M. Shoemaker,[77] S. ShyamSundar,[61] K. Siellez,[77] M. Sieniawska,[54] D. Sigg,[45] A. D. Silva,[13] L. P. Singer,[80] N. Singh,[74] A. Singhal,[14,32] A. M. Sintes,[100] S. Sitmukhambetov,[105] V. Skliris,[68] B. J. J. Slagmolen,[21] T. J. Slaven-Blair,[63] J. R. Smith,[26] R. J. E. Smith,[6] S. Somala,[167] E. J. Son,[139] B. Sorazu,[44] F. Sorrentino,[60] T. Souradeep,[3] E. Sowell,[83] A. P. Spencer,[44] A. K. Srivastava,[108] V. Srivastava,[42] K. Staats,[59] C. Stachie,[65] M. Standke,[8,9] D. A. Steer,[27] M. Steinke,[8,9] J. Steinlechner,[141,44] S. Steinlechner,[141] D. Steinmeyer,[8,9] S. P. Stevenson,[152] D. Stocks,[49] R. Stone,[105] D. J. Stops,[11] K. A. Strain,[44] G. Stratta,[72,73] S. E. Strigin,[62] A. Strunk,[45] R. Sturani,[168] A. L. Stuver,[169] V. Sudhir,[12] T. Z. Summerscales,[170] L. Sun,[1] S. Sunil,[108] J. Suresh,[3] P. J. Sutton,[68] B. L. Swinkels,[37] M. J. Szczepańczyk,[34] M. Tacca,[37] S. C. Tait,[44] C. Talbot,[6] D. Talukder,[70] D. B. Tanner,[48] M. Tápai,[124] A. Taracchini,[36] J. D. Tasson,[94] R. Taylor,[1] R. Tenorio,[100] F. Thies,[8,9] M. Thomas,[7] P. Thomas,[45] S. R. Thondapu,[61] K. A. Thorne,[7] E. Thrane,[6] Shubhanshu Tiwari,[113,96] Srishti Tiwari,[125] V. Tiwari,[68] K. Toland,[44] M. Tonelli,[18,19] Z. Tornasi,[44] A. Torres-Forné,[171] C. I. Torrie,[1] D. Töyrä,[11] F. Travasso,[28,41] G. Traylor,[7] M. C. Tringali,[74] A. Trovato,[27] L. Trozzo,[172,19] R. Trudeau,[1] K. W. Tsang,[37] M. Tse,[12] R. Tso,[46] L. Tsukada,[81] D. Tsuna,[81] D. Tuyenbayev,[105] K. Ueno,[81] D. Ugolini,[173] C. S. Unnikrishnan,[125] A. L. Urban,[2] S. A. Usman,[68] H. Vahlbruch,[9] G. Vajente,[1] G. Valdes,[2] N. van Bakel,[37] M. van Beuzekom,[37] J. F. J. van den Brand,[75,37] C. Van Den Broeck,[37,174] D. C. Vander-Hyde,[42] J. V. van Heijningen,[63] L. van der Schaaf,[37] A. A. van Veggel,[44] M. Vardaro,[51,52] V. Varma,[46] S. Vass,[1] M. Vasúth,[47] A. Vecchio,[11] G. Vedovato,[52] J. Veitch,[44] P. J. Veitch,[55] K. Venkateswara,[163] G. Venugopalan,[1] D. Verkindt,[33] F. Vetrano,[72,73] A. Viceré,[72,73] A. D. Viets,[23] D. J. Vine,[164] J.-Y. Vinet,[65] S. Vitale,[12] T. Vo,[42] H. Vocca,[40,41] C. Vorvick,[45] S. P. Vyatchanin,[62] A. R. Wade,[1] L. E. Wade,[117] M. Wade,[117] R. Walet,[37] M. Walker,[26] L. Wallace,[1] S. Walsh,[23] G. Wang,[14,19] H. Wang,[11] J. Z. Wang,[127] W. H. Wang,[105] Y. F. Wang,[91] R. L. Ward,[21] Z. A. Warden,[34] J. Warner,[45] M. Was,[33] J. Watchi,[101] B. Weaver,[45] L.-W. Wei,[8,9] M. Weinert,[8,9] A. J. Weinstein,[1] R. Weiss,[12] G. Weldon,[127] F. Wellmann,[8,9] L. Wen,[63] E. K. Wessel,[17] P. Weßels,[8,9] J. W. Westhouse,[34] K. Wette,[21] J. T. Whelan,[58] B. F. Whiting,[48] C. Whittle,[12] D. M. Wilken,[8,9] D. Williams,[44] A. R. Williamson,[129,37] J. L. Willis,[1] B. Willke,[8,9] M. H. Wimmer,[8,9] W. Winkler,[8,9] C. C. Wipf,[1] H. Wittel,[8,9] G. Woan,[44] J. Woehler,[8,9] J. K. Wofford,[58] J. Worden,[45] J. L. Wright,[44] D. S. Wu,[8,9] D. M. Wysocki,[58] L. Xiao,[1] H. Yamamoto,[1] C. C. Yancey,[76]

L. Yang,[116] M. J. Yap,[21] M. Yazback,[48] D. W. Yeeles,[68] Hang Yu,[12] Haocun Yu,[12] S. H. R. Yuen,[91] M. Yvert,[33] A. K. Zadrożny,[105,115] M. Zanolin,[34] T. Zelenova,[28] J.-P. Zendri,[52] M. Zevin,[59] J. Zhang,[63] L. Zhang,[1] T. Zhang,[44] C. Zhao,[63] M. Zhou,[59] Z. Zhou,[59] X. J. Zhu,[6] M. E. Zucker,[1,12] and J. Zweizig[1]

(LIGO Scientific Collaboration and Virgo Collaboration)

A. Pisarski[132]

[1]*LIGO, California Institute of Technology, Pasadena, California 91125, USA*
[2]*Louisiana State University, Baton Rouge, Louisiana 70803, USA*
[3]*Inter-University Centre for Astronomy and Astrophysics, Pune 411007, India*
[4]*Università di Salerno, Fisciano, I-84084 Salerno, Italy*
[5]*INFN, Sezione di Napoli, Complesso Universitario di Monte S.Angelo, I-80126 Napoli, Italy*
[6]*OzGrav, School of Physics & Astronomy, Monash University, Clayton 3800, Victoria, Australia*
[7]*LIGO Livingston Observatory, Livingston, Louisiana 70754, USA*
[8]*Max Planck Institute for Gravitational Physics (Albert Einstein Institute), D-30167 Hannover, Germany*
[9]*Leibniz Universität Hannover, D-30167 Hannover, Germany*
[10]*University of Cambridge, Cambridge CB2 1TN, United Kingdom*
[11]*University of Birmingham, Birmingham B15 2TT, United Kingdom*
[12]*LIGO, Massachusetts Institute of Technology, Cambridge, Massachusetts 02139, USA*
[13]*Instituto Nacional de Pesquisas Espaciais, 12227-010 São José dos Campos, São Paulo, Brazil*
[14]*Gran Sasso Science Institute (GSSI), I-67100 L'Aquila, Italy*
[15]*INFN, Laboratori Nazionali del Gran Sasso, I-67100 Assergi, Italy*
[16]*International Centre for Theoretical Sciences, Tata Institute of Fundamental Research, Bengaluru 560089, India*
[17]*NCSA, University of Illinois at Urbana-Champaign, Urbana, Illinois 61801, USA*
[18]*Università di Pisa, I-56127 Pisa, Italy*
[19]*INFN, Sezione di Pisa, I-56127 Pisa, Italy*
[20]*Departamento de Astronomía y Astrofísica, Universitat de València, E-46100 Burjassot, València, Spain*
[21]*OzGrav, Australian National University, Canberra, Australian Capital Territory 0200, Australia*
[22]*Laboratoire des Matériaux Avancés (LMA), CNRS/IN2P3, F-69622 Villeurbanne, France*
[23]*University of Wisconsin-Milwaukee, Milwaukee, Wisconsin 53201, USA*
[24]*SUPA, University of Strathclyde, Glasgow G1 1XQ, United Kingdom*
[25]*LAL, Université Paris-Sud, CNRS/IN2P3, Université Paris-Saclay, F-91898 Orsay, France*
[26]*California State University Fullerton, Fullerton, California 92831, USA*
[27]*APC, AstroParticule et Cosmologie, Université Paris Diderot, CNRS/IN2P3, CEA/Irfu, Observatoire de Paris, Sorbonne Paris Cité, F-75205 Paris Cedex 13, France*
[28]*European Gravitational Observatory (EGO), I-56021 Cascina, Pisa, Italy*
[29]*Chennai Mathematical Institute, Chennai 603103, India*
[30]*Università di Roma Tor Vergata, I-00133 Roma, Italy*
[31]*INFN, Sezione di Roma Tor Vergata, I-00133 Roma, Italy*
[32]*INFN, Sezione di Roma, I-00185 Roma, Italy*
[33]*Laboratoire d'Annecy de Physique des Particules (LAPP), Université Grenoble Alpes, Université Savoie Mont Blanc, CNRS/IN2P3, F-74941 Annecy, France*
[34]*Embry-Riddle Aeronautical University, Prescott, Arizona 86301, USA*
[35]*Montclair State University, Montclair, New Jersey 07043, USA*
[36]*Max Planck Institute for Gravitational Physics (Albert Einstein Institute), D-14476 Potsdam-Golm, Germany*
[37]*Nikhef, Science Park 105, 1098 XG Amsterdam, The Netherlands*
[38]*Korea Institute of Science and Technology Information, Daejeon 34141, South Korea*
[39]*West Virginia University, Morgantown, West Virginia 26506, USA*
[40]*Università di Perugia, I-06123 Perugia, Italy*
[41]*INFN, Sezione di Perugia, I-06123 Perugia, Italy*
[42]*Syracuse University, Syracuse, New York 13244, USA*
[43]*University of Minnesota, Minneapolis, Minnesota 55455, USA*
[44]*SUPA, University of Glasgow, Glasgow G12 8QQ, United Kingdom*
[45]*LIGO Hanford Observatory, Richland, Washington 99352, USA*
[46]*Caltech CaRT, Pasadena, California 91125, USA*
[47]*Wigner RCP, RMKI, H-1121 Budapest, Konkoly Thege Miklós út 29-33, Hungary*
[48]*University of Florida, Gainesville, Florida 32611, USA*

[49]Stanford University, Stanford, California 94305, USA
[50]Università di Camerino, Dipartimento di Fisica, I-62032 Camerino, Italy
[51]Università di Padova, Dipartimento di Fisica e Astronomia, I-35131 Padova, Italy
[52]INFN, Sezione di Padova, I-35131 Padova, Italy
[53]Montana State University, Bozeman, Montana 59717, USA
[54]Nicolaus Copernicus Astronomical Center, Polish Academy of Sciences, 00-716 Warsaw, Poland
[55]OzGrav, University of Adelaide, Adelaide, South Australia 5005, Australia
[56]Theoretisch-Physikalisches Institut, Friedrich-Schiller-Universität Jena, D-07743 Jena, Germany
[57]INFN, Sezione di Milano Bicocca, Gruppo Collegato di Parma, I-43124 Parma, Italy
[58]Rochester Institute of Technology, Rochester, New York 14623, USA
[59]Center for Interdisciplinary Exploration & Research in Astrophysics (CIERA), Northwestern University, Evanston, Illinois 60208, USA
[60]INFN, Sezione di Genova, I-16146 Genova, Italy
[61]RRCAT, Indore, Madhya Pradesh 452013, India
[62]Faculty of Physics, Lomonosov Moscow State University, Moscow 119991, Russia
[63]OzGrav, University of Western Australia, Crawley, Western Australia 6009, Australia
[64]Department of Astrophysics/IMAPP, Radboud University Nijmegen, P.O. Box 9010, 6500 GL Nijmegen, The Netherlands
[65]Artemis, Université Côte d'Azur, Observatoire Côte d'Azur, CNRS, CS 34229, F-06304 Nice Cedex 4, France
[66]Physik-Institut, University of Zurich, Winterthurerstrasse 190, 8057 Zurich, Switzerland
[67]Univ Rennes, CNRS, Institut FOTON—UMR6082, F-3500 Rennes, France
[68]Cardiff University, Cardiff CF24 3AA, United Kingdom
[69]Washington State University, Pullman, Washington 99164, USA
[70]University of Oregon, Eugene, Oregon 97403, USA
[71]Laboratoire Kastler Brossel, Sorbonne Université, CNRS, ENS-Université PSL, Collège de France, F-75005 Paris, France
[72]Università degli Studi di Urbino "Carlo Bo", I-61029 Urbino, Italy
[73]INFN, Sezione di Firenze, I-50019 Sesto Fiorentino, Firenze, Italy
[74]Astronomical Observatory Warsaw University, 00-478 Warsaw, Poland
[75]VU University Amsterdam, 1081 HV Amsterdam, The Netherlands
[76]University of Maryland, College Park, Maryland 20742, USA
[77]School of Physics, Georgia Institute of Technology, Atlanta, Georgia 30332, USA
[78]Université Claude Bernard Lyon 1, F-69622 Villeurbanne, France
[79]Università di Napoli 'Federico II', Complesso Universitario di Monte S.Angelo, I-80126 Napoli, Italy
[80]NASA Goddard Space Flight Center, Greenbelt, Maryland 20771, USA
[81]RESCEU, University of Tokyo, Tokyo 113-0033, Japan
[82]Tsinghua University, Beijing 100084, China
[83]Texas Tech University, Lubbock, Texas 79409, USA
[84]The University of Mississippi, University, Mississippi 38677, USA
[85]Museo Storico della Fisica e Centro Studi e Ricerche "Enrico Fermi", I-00184 Roma, Italyrico Fermi, I-00184 Roma, Italy
[86]The Pennsylvania State University, University Park, Pennsylvania 16802, USA
[87]National Tsing Hua University, Hsinchu City, 30013 Taiwan, Republic of China
[88]Charles Sturt University, Wagga, Wagga, New South Wales 2678, Australia
[89]Canadian Institute for Theoretical Astrophysics, University of Toronto, Toronto, Ontario M5S 3H8, Canada
[90]University of Chicago, Chicago, Illinois 60637, USA
[91]The Chinese University of Hong Kong, Shatin, NT, Hong Kong
[92]Seoul National University, Seoul 08826, South Korea
[93]Pusan National University, Busan 46241, South Korea
[94]Carleton College, Northfield, Minnesota 55057, USA
[95]INAF, Osservatorio Astronomico di Padova, I-35122 Padova, Italy
[96]INFN, Trento Institute for Fundamental Physics and Applications, I-38123 Povo, Trento, Italy
[97]Dipartimento di Fisica, Università degli Studi di Genova, I-16146 Genova, Italy
[98]OzGrav, University of Melbourne, Parkville, Victoria 3010, Australia
[99]Columbia University, New York, New York 10027, USA
[100]Universitat de les Illes Balears, IAC3–IEEC, E-07122 Palma de Mallorca, Spain
[101]Université Libre de Bruxelles, Brussels 1050, Belgium
[102]Sonoma State University, Rohnert Park, California 94928, USA

[103]*Departamento de Matemáticas, Universitat de València, E-46100 Burjassot, València, Spain*
[104]*University of Rhode Island, Kingston, Rhode Island 02881, USA*
[105]*The University of Texas Rio Grande Valley, Brownsville, Texas 78520, USA*
[106]*Bellevue College, Bellevue, Washington 98007, USA*
[107]*MTA-ELTE Astrophysics Research Group, Institute of Physics, Eötvös University, Budapest 1117, Hungary*
[108]*Institute for Plasma Research, Bhat, Gandhinagar 382428, India*
[109]*The University of Sheffield, Sheffield S10 2TN, United Kingdom*
[110]*IGFAE, Campus Sur, Universidade de Santiago de Compostela, 15782 Spain*
[111]*Dipartimento di Scienze Matematiche, Fisiche e Informatiche, Università di Parma, I-43124 Parma, Italy*
[112]*California State University, Los Angeles, 5151 State University Drive, Los Angeles, California 90032, USA*
[113]*Università di Trento, Dipartimento di Fisica, I-38123 Povo, Trento, Italy*
[114]*Università di Roma "La Sapienza", I-00185 Roma, Italy*
[115]*NCBJ, 05-400 Świerk-Otwock, Poland*
[116]*Colorado State University, Fort Collins, Colorado 80523, USA*
[117]*Kenyon College, Gambier, Ohio 43022, USA*
[118]*Christopher Newport University, Newport News, Virginia 23606, USA*
[119]*National Astronomical Observatory of Japan, 2-21-1 Osawa, Mitaka, Tokyo 181-8588, Japan*
[120]*Observatori Astronòmic, Universitat de València, E-46980 Paterna, València, Spain*
[121]*School of Mathematics, University of Edinburgh, Edinburgh EH9 3FD, United Kingdom*
[122]*Institute Of Advanced Research, Gandhinagar 382426, India*
[123]*Indian Institute of Technology Bombay, Powai, Mumbai 400 076, India*
[124]*University of Szeged, Dóm tér 9, Szeged 6720, Hungary*
[125]*Tata Institute of Fundamental Research, Mumbai 400005, India*
[126]*INAF, Osservatorio Astronomico di Capodimonte, I-80131 Napoli, Italy*
[127]*University of Michigan, Ann Arbor, Michigan 48109, USA*
[128]*American University, Washington, DC 20016, USA*
[129]*GRAPPA, Anton Pannekoek Institute for Astronomy and Institute of High-Energy Physics, University of Amsterdam, Science Park 904, 1098 XH Amsterdam, The Netherlands*
[130]*Delta Institute for Theoretical Physics, Science Park 904, 1090 GL Amsterdam, The Netherlands*
[131]*Directorate of Construction, Services & Estate Management, Mumbai 400094 India*
[132]*University of Białystok, 15-424 Białystok, Poland*
[133]*King's College London, University of London, London WC2R 2LS, United Kingdom*
[134]*University of Southampton, Southampton SO17 1BJ, United Kingdom*
[135]*University of Washington Bothell, Bothell, Washington 98011, USA*
[136]*Institute of Applied Physics, Nizhny Novgorod 603950, Russia*
[137]*Ewha Womans University, Seoul 03760, South Korea*
[138]*Inje University Gimhae, South Gyeongsang 50834, South Korea*
[139]*National Institute for Mathematical Sciences, Daejeon 34047, South Korea*
[140]*Ulsan National Institute of Science and Technology, Ulsan 44919, South Korea*
[141]*Universität Hamburg, D-22761 Hamburg, Germany*
[142]*Maastricht University, P.O. Box 616, 6200 MD Maastricht, The Netherlands*
[143]*Institute of Mathematics, Polish Academy of Sciences, 00656 Warsaw, Poland*
[144]*Cornell University, Ithaca, New York 14850, USA*
[145]*Hillsdale College, Hillsdale, Michigan 49242, USA*
[146]*Hanyang University, Seoul 04763, South Korea*
[147]*Korea Astronomy and Space Science Institute, Daejeon 34055, South Korea*
[148]*NASA Marshall Space Flight Center, Huntsville, Alabama 35811, USA*
[149]*Dipartimento di Matematica e Fisica, Università degli Studi Roma Tre, I-00146 Roma, Italy*
[150]*INFN, Sezione di Roma Tre, I-00146 Roma, Italy*
[151]*ESPCI, CNRS, F-75005 Paris, France*
[152]*OzGrav, Swinburne University of Technology, Hawthorn VIC 3122, Australia*
[153]*University of Portsmouth, Portsmouth PO1 3FX, United Kingdom*
[154]*Southern University and A&M College, Baton Rouge, Louisiana 70813, USA*
[155]*College of William and Mary, Williamsburg, Virginia 23187, USA*
[156]*Centre Scientifique de Monaco, 8 quai Antoine Ier, MC-98000, Monaco*
[157]*Indian Institute of Technology Madras, Chennai 600036, India*
[158]*IISER-Kolkata, Mohanpur, West Bengal 741252, India*

[159]Whitman College, 345 Boyer Avenue, Walla Walla, Washington 99362, USA
[160]Université de Lyon, F-69361 Lyon, France
[161]Hobart and William Smith Colleges, Geneva, New York 14456, USA
[162]Janusz Gil Institute of Astronomy, University of Zielona Góra, 65-265 Zielona Góra, Poland
[163]University of Washington, Seattle, Washington 98195, USA
[164]SUPA, University of the West of Scotland, Paisley PA1 2BE, United Kingdom
[165]Indian Institute of Technology, Gandhinagar, Ahmedabad, Gujarat 382424, India
[166]Université de Montréal/Polytechnique, Montreal, Quebec H3T 1J4, Canada
[167]Indian Institute of Technology Hyderabad, Sangareddy, Khandi, Telangana 502285, India
[168]International Institute of Physics, Universidade Federal do Rio Grande do Norte, Natal RN 59078-970, Brazil
[169]Villanova University, 800 Lancaster Avenue, Villanova, Pennsylvania 19085, USA
[170]Andrews University, Berrien Springs, Michigan 49104, USA
[171]Max Planck Institute for Gravitationalphysik (Albert Einstein Institute), D-14476 Potsdam-Golm, Germany
[172]Università di Siena, I-53100 Siena, Italy
[173]Trinity University, San Antonio, Texas 78212, USA
[174]Van Swinderen Institute for Particle Physics and Gravity, University of Groningen, Nijenborgh 4, 9747 AG Groningen, The Netherlands

[†]Deceased.